PROCEEDINGS, 49th Workshop on Geothermal Reservoir Engineering
Stanford University, Stanford, California, February 12-14, 2024
SGP-TR-227

Research Development for Geothermal Heat Flux Understanding and Evaluation by Numerical Modeling of the Ground Surface Heat Balance System in Mount Meager Area during Snow Covering Period

Yu Zheng, Yue Zhuo, Wanju Yuan*, Zhuoheng Chen and Gang Zhao*

University of Regina, Geological Survey of Canada Calgary

zheng27y@uregina.ca, yzw986@uregina.ca, wanju.yuan@nrcan-rncan.gc.ca, zhuoheng.chen@nrcan-rncan.gc.ca, gang.zhao@uregina.ca

* Corresponding author

Keywords: Mount Meager geothermal field, heat flux, temperature time series, temperature profile, temporal temperature mapping, heat source, snow-covering period, snow-curtain, geostatistical estimation, numerical modeling

ABSTRACT

Geothermal resource assessment has been conducted by the Geological Survey of Canada (GSC) in the Garibaldi Geothermal Volcanic Belt area in supporting the Geoscience for New Energy Supply Program. Near-surface ground temperature datasets were collected using new geothermal exploration methods in Mount Meager and Mount Cayley geothermal areas during the 2021 and 2022 summer fieldwork seasons. Research work is ongoing to analyze and evaluate the temperature records by building numerical models of heat balance of the shallow underground and analytical heat conservation models. The objective of this study is to undertake a numerical modeling approach to gain a better understanding of heat balance system during the winter snow-covering period and analyze the temperature data for calculating the subsurface geothermal heat flux. The results from this work provide insights for analyzing field data and eventually benefit the geothermal resources assessment in this area. The ground temperature is affected by many environmental and soil properties and physical processes, such as geothermal heat flux, solar radiation, water evaporation and condensation, snowmelt, rain and advective heat flux by the movement of subsurface ground water flow. From the collected ground surface temperature datasets from temperature sensors placed in the topsoil of Mount Meager geothermal field, a relatively stable temperature period is generally identifiable during the snow covering (snow-curtain) period, which may help eliminate major environmental effects and reveal the contribution of the geothermal energy heat flux. To better understanding the temperature variation in the datasets, the 22 temperature time series recorded in the 2020-21 winter period were organized in three groups and presented accordingly, depending on the range of the measured temperature and the trends of variation. Then Simple and Ordinary Kriging (SK and OK) were applied to generate temperature maps at equal spaced temporal points to reveal the dynamics of temperature variation of the Mount Meager geothermal field. It is found that our general understanding based on the categorized sampled data is consistent with the insights revealed through the temporal temperature field mapping and that the heat sources hidden underneath the covering snow can be clearly identified through temporal geostatistical mapping. In order to achieve a better matching and consider the complexity of the problem, a simplified 2D numerical model using COMSOL multiphysics software was constructed to help identify the heat flux range and the temperature distribution for the targeted area. The results show the sensitivities of various geological and environmental factors that affect the ground temperature. We believe that the output from this research provide insights from data analysis and interpretation, and will be of importance for the future research work of the Mount Meager geothermal field. The recommendation for future research is to build an accurate multiphysics model that can simultaneously consider the snow accumulating and melting processes under more realistic conditions.

1. INTRODUCTION

Mount Meager is located in southwestern British Columbia, Canada. This volcano-hosted high temperature area has been studied for geothermal energy resources for decades. However, the geothermal project has been on pause since the global economic crisis and insufficient water producing rate and financial support. Although Geoscience BC made a large volume of surface and underground geothermal resource data publicly available (Geoscience BC,2017), the assessment has just been recently conducted by the Geological Survey of Canada (GSC) in the Garibaldi Geothermal Volcanic Belt area to support the Geoscience for New Energy Supply (GNES) program. Near-surface ground temperature datasets were collected using new geothermal exploration methods in Mount Meager and Mount Cayley geothermal areas during the 2021 and 2022 summer fieldwork seasons (Chen et al. 2023). This study investigated the temperature time series recorded in this geothermal prospect area over a two-year duration in 2020 and 2021 and tried to find out a way to build proper models to analyze the collected field temperature data.

The development of the snow melt model has a long history, and it has been studied for years in literature. In general, there are two types of methods that were used for snow modelling, the temperature index method and the energy balance method. The temperature index method, also called degree-day model, shows the relationship between snow/ice melt and air temperature. Since air temperature is the most convenient data to collect, this model has been widely used for snow/ice melt computation in many areas, such as snow modeling, ice dynamic modeling, and climate sensitivity studies (Agnihotri and Coulibaly, 2020). The mathematical expression of this method is

$$M = (T_a - T_m) \cdot DDF \quad (1)$$

where M, T_a, T_m, DDF are snow/ice melt rate, air temperature, melt temperature of snow/ice, and degree-day factor respectively (Agnihotri and Coulibaly, 2020). The universal equation for temperature index is the depth of melt snow equals melt factor times the difference between air temperature and melt temperature. This equation was established based on the assumption that snow melt rate is linearly related to daily temperature. This method is relatively easy to apply because of the limited number of parameters involved. However, the accuracy of the model applied in various areas may be a concern due to challenge in the consistency of parameters used.

The energy balance snow melting model calculated snowmelt based on the energy exchange among snow covering layer, the subsurface soil and rock layers, and the environment. It needs to derive an energy balance equation into the process of snow accumulation to build a snow runoff simulation. Singh (2009) presented a general theoretical expression of this model in graphics, as shown in **Figure 1** (Singh et al., 2009).

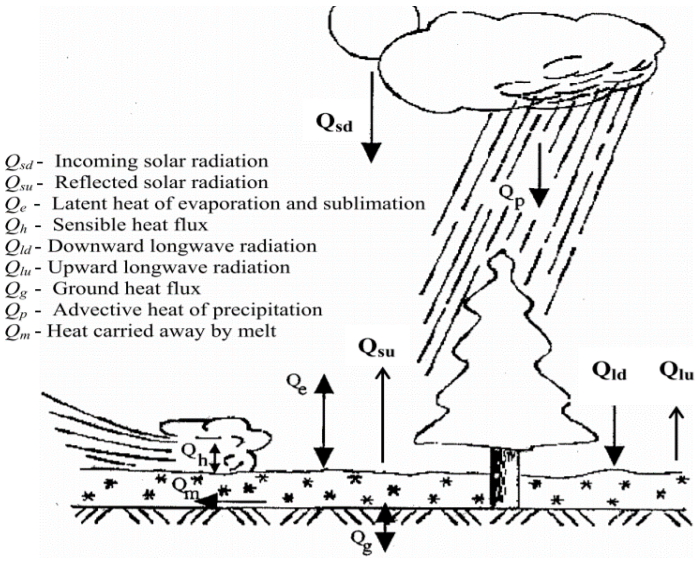

Figure 1: Energy fluxes involved in an energy balance snow melting model (Sigh, 2009).

This figure shows the basic concept of the energy balance snow melting model. In this model, heat fluxes were considered in snow accumulation and snowmelt processes. The heat for snowmelt is equal to the sum of solar radiation, latent heat of snow evaporation, sensible heat flux, advective heat of precipitation, and geothermal ground heat flux from heat source. The complete energy balance snow melting modeling for Mount Meager area can be very difficult to attain because of the limitation in available information and moreover, the complexity of the problem.

In this research, we have chosen COMSOL Multiphysics to conduct a simplified simulation study. This versatile software package is widely employed to simulate and solve problems across various engineering and scientific domains, with a particular focus on heat transfer — one of its key applications. The Heat Transfer Module within COMSOL offers a robust set of tools for simulating heat transfer phenomena in diverse applications, covering conduction, convection, radiation, and phase change (COMSOL Multiphysics, 2022).

In our study, due to the complexity of the problem and the limited field data, the energy model between snow covering layer and soil layer is considered and an overall representative ground cold-water flow velocity is applied to roughly integrate the influence of the other factors that have no related information collected/measured. Therefore, this work provided a simplified qualitative simulation work focusing on different geothermal gradients and thermal properties in soil and rock layers. The energy balance system is modeled as

$$\boldsymbol{q} = -d_z k_{eff} \nabla T \tag{2}$$

$$d_z\left(\rho C_p\right)_{eff} \frac{\partial T}{\partial t} + d_z \rho_f C_{p,f} \mathbf{u} \cdot \nabla T + \nabla \cdot \boldsymbol{q} = d_z Q + q_0 + d_z Q_p + d_z Q_{vd} + d_z Q_{geo} \tag{3}$$

where, $\mathbf{q}$, d_z, k_{eff}, ∇T, ρ, C_p, ρ_f, $C_{p,f}$, $\mathbf{u}$ are conductive heat flux vector, thickness of domain in the out-of-plane direction, effective thermal conductivity, temperature gradient, density of media, specific heat capacity at constant pressure, fluid density, fluid specific heat capacity at constant pressure, fluid velocity vector, respectively. And Q, q_0, Q_p, Q_{vd}, and Q_{geo} are heat source, inward heat flux, point heat source, heat dissipation by viscous flow, and geothermal heat source, respectively.

The field temperature data collected from the Mount Meager geothermal site have presented challenge in terms of trying to understand the information contained within the dataset. We have applied geostatistics techniques to help improve our understanding. Geostatistics is a statistical branch focused on spatial and spatiotemporal datasets. It was initially developed to examine ore grade distributions in

mining during the 1950s and 1960s (Krige 1951; Matheron 1963). It has since been utilized in a variety of fields, including petroleum, hydrogeology, meteorology, oceanography, geochemistry, environmental sciences, and agriculture (Kelkar et al., 2002; Kitanidis 1997; M A Oliver 1987; Margaret A Oliver 2010; Paz-Ferreiro et al., 2010; Renard et al., 2005). In exploring geothermal energy, geostatistics is crucial in leveraging statistical techniques to assess and predict the geothermal distribution of geological factors. Its applications span from resource identification to assessment and prediction (Vidal and Archer 2015; Witter et al., 2019). In this paper, the Simple Kriging (SK) and Ordinary Kriging (OK) under isotropy variogram situation were applied in extrapolating the data due to the complexity and the challenge of understanding the whole dataset and the SGeMS (Stanford Geostatistical Modeling Software) was used to conduct the calculation.

For clarity, the collected sensor temperature measurement is called temperature time series in this work, the simulation result generated through COMSOL modeling with fine grid scheme is named temperature profile because it can be output depending on time interval specified, and the temperature outcome estimated by geostatistics is described as temperature mapping for the field studied.

2. DATA AND METHODS

2.1 Temperature Data Collection

The temperature data from Mount Meager was collected using temperature sensors at the 22 distinct sites, the geological locations of them are illustrated in google satellite image, shown in **Figure 2**. All temperature sensors were placed around 10 centimeters below the ground soil surface for each site to avoid direct solar radiation and weather fluctuation. The sensors were strategically planted near the trail, and their elevations generally descend from site 1 to site 22. The elevation of site 1 is the highest at 1386m and the elevation of site 22 is the lowest at 593m. The ultimate snow melting date at sensor 1 should be later in time than those of the other sensors because sensor 1 locates at the highest and coldest place in the dataset. And the Sensor 21 should have the shortest snow cover period because a hot spring is near its proximity. All sensors have the same measurement frequency of one temperature point every 30 minutes for one year duration, starting from September 20th, 2020.

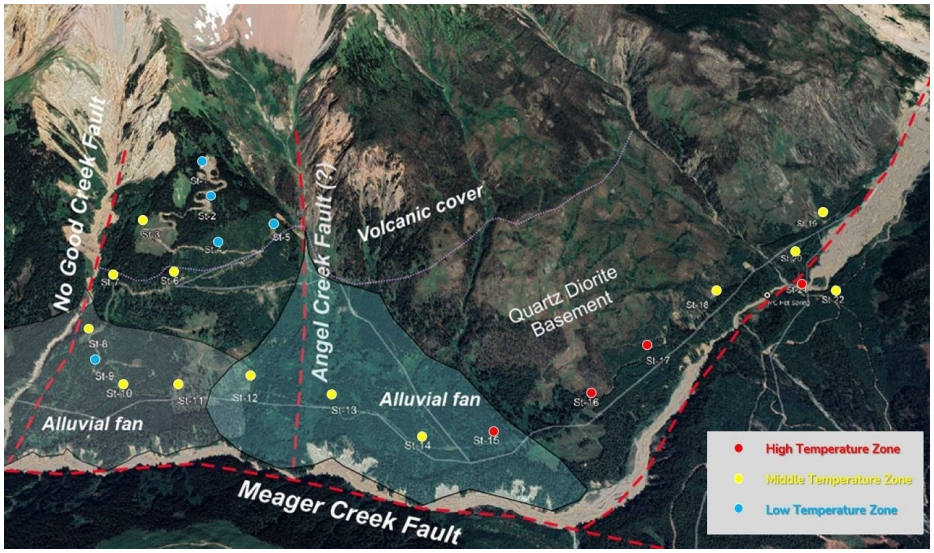

Figure 2: Google satellite image for Mount Meager geothermal prospect area with categorized sensor sites identified, modified after Chen et al. (2022).

2.2 Temperature Data Analysis

All the temperature data logs were collected and organized in Excel software to plot the graph. For a clear presentation, the Data Legend Name format is structured as sensor# - bury depth (cm) – moisture percentage – elevation (m) – days of snow-covering period on the right-hand side of the graph. For example, sensor 1 is represented as 1A-2-31-1386-211. The letter "A" represents the 2020-2021 winter. As the project is focused on the snow covering period, the plot in **Figure 3** below exclusively illustrates temperature changes in winter for sensors 1 to 22 from the beginning to the end of the winter in 2020-2021.

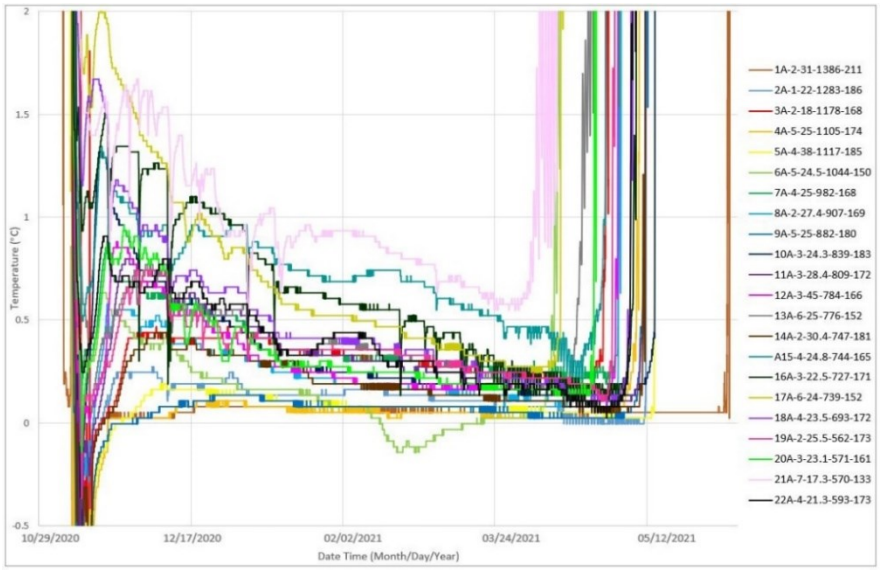

Figure 3: Mount Meager field temperature data from all the 22 sites collected in 2020-2021 winter.

In the early stages of winter, temperatures drop below 0 °C as the sensors expose to the air in the soil before snowfall. Consequently, the sensors measure the surrounding environment's air temperature. Subsequently, the snowfall process absorbs heat from the surroundings, leading to a further drop in air temperature. Following snow precipitation and accumulation, the temperatures measured by the sensors gradually reach around 0 °C and maintain near the freezing point. This occurs because the accumulated snow acts as insulation, blocking heat exchange with external air and reflecting sunlight. This snow-covered stage is termed the snow-curtain period, marked by the complete coverage of the topsoil surface under snow. During this phase, the temperature reaches an equilibrium, with the snow temperature remaining constant around 0 °C. The snow-curtain effect, which involves the release or absorption of latent heat from the snow, slows the freezing process. As a result, ground temperatures remain near 0 °C, while air temperatures may fluctuate. Towards the end of winter, as air temperatures rise, the snow begins to melt, initiating the snow melting period. The trends of winter temperature dynamics shown in Figure 3 can be identified in three main categories: Category 1, representing high-temperature ranges; Category 2, representing intermediate-temperature ranges; and Category 3, representing low-temperature ranges, as presented in the following figures from **Figures 4 to 6**. The categorized temperature data with their corresponding sensor sites are marked and identified in Figure 2 with different colors on the spots.

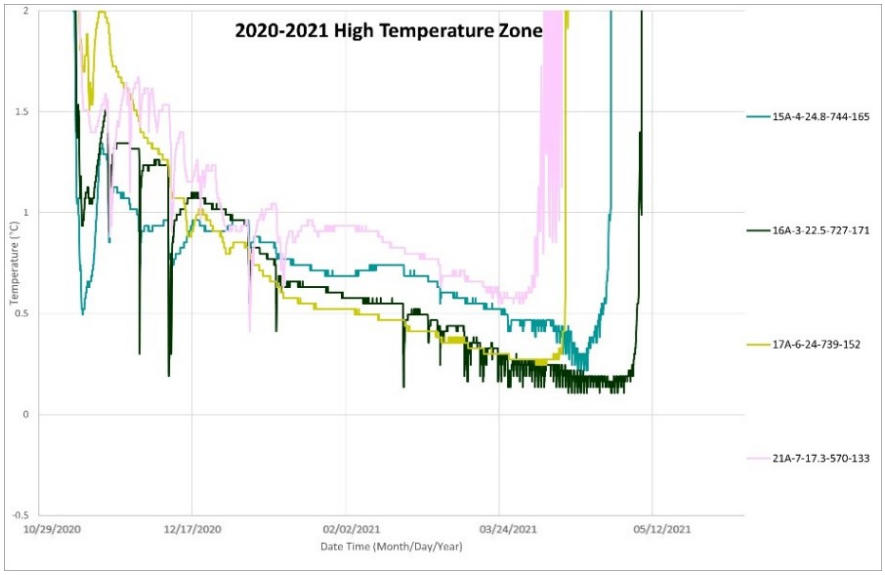

Figure 4: Category 1 temperature dynamics from sensors in high temperature zone in 2020-2021 winter.

As shown in Figure 4, Category 1 comprises sensors at site 15, 16, 17, and 21, displaying relatively high temperatures during the winter. The sensor positioned at site 21 consistently recorded the highest temperature, especially noticeable during snow accumulation. Moreover,

this sensor experiences the earliest snow melting among all. The location of sensor 21 is near a hot spring, so the result is likely influenced by the heat flux from the hot spring and the temperature is therefore higher than other sensors.

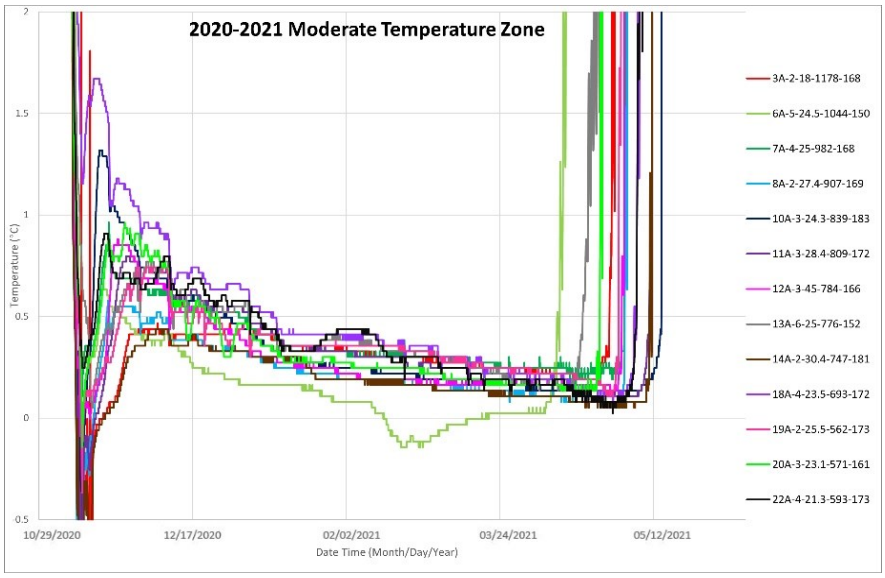

Figure 5: Category 2 temperature dynamics from sensors in the moderate temperature zone in 2020-2021 winter.

As shown in Figure 5, Category 2 encompasses sensors in the moderate temperature zone, all temperature time series exhibit a very similar pattern. However, sensors at sites 10 and 11 recorded unusually high temperatures at the beginning of winter. Additionally, sensor at site 13 experiences early snow melting compared to other sensor locations. These sensors, along with those at sites 15, 16, and 17, are situated at the foothill of the mountain, suggesting a possible heat flow beneath the ground in this area. The sensor at site 3, situated in a high elevation area that is expected to experience a similar later melting stage as other high elevation sites in the low temperature zone shown in Figure 6. Moreover, site 3 had the lowest soil moisture (18%) among all sites. Apparently, the location of sensor 3 received more solar radiation than sensors in other locations as it recorded the highest day temperature in snow free season. The possible reason is that there is not much vegetation in this area and sunlight directly heats the surface to evaporate a large amount of water in the soil. The sensor at site 22 consistently shows relatively high temperatures, which are likely influenced by the nearby hot spring located near site 21. Moreover, the temperature time series of sensor 6 is unique because it was going below 0 °C during the later period of the winter. Site 6 also starts to melt at an early stage. This uniqueness may be caused by fully saturated underground water moving downwards through, lowering down the temperature.

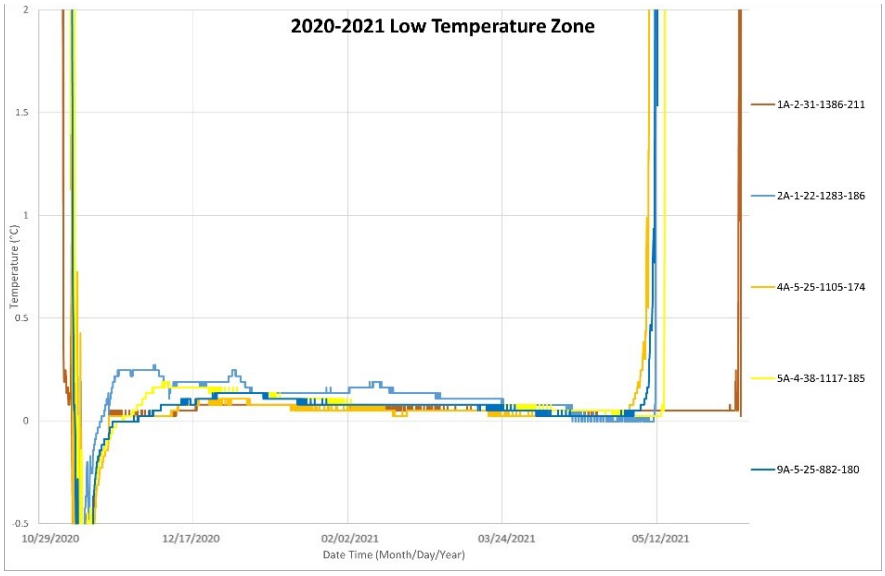

Figure 6: Category 3 temperature dynamics for sensors in the low temperature zone in 2020-2021 winter.

In the category 3 as shown in Figure 6, temperature time series during the snow-curtain period consistently fall within the low-temperature zone, close to 0 °C. The majority of these temperature time series exhibit a similar trend, with the only noticeable difference being that

sensor 1 experiences snow melting at a later time compared to the other sensors. This delay can be attributed to the elevated position of sensor at site 1, located in the coldest area due to its highest elevation. Additionally, sensors 2, 4, and 5 display similar trends in the measured data during this period.

As seen from Figure 2, the categorization of the temperature curves into three groups in terms of high, moderate and low temperature zones makes sense, because the high temperature curves are near the surface geothermal heat sources, the moderate curves are likely recoded by sensors located at areas with relatively larger ground water flow around the alluvial fan area near the foot of the Mount Meager, and lastly the low temperature curves are captured by the sensors positioned at sites with higher elevation where a colder ground water flow is expected.

2.3 COMSOL Multiphysics Model

For this study, we have implemented COMSOL Multiphysics software to simulate this complicated system involving snowmelt, ground cold-water flow, and subsurface geothermal heat transfer processes. A simplified two-dimensional (2D) model to ideally represent the Mount Meager field using COMSOL Multiphysics has been built, as shown in **Figure 7**. The Model Wizard of COMSOL for 2D space dimension option was used to construct the model for this simulation. The general model consists of a 100 m thick rock layer, a 60 m thick soil layer, and a 2 m thick snow-curtain layer. The width of the model is 100 m. The sensor is placed 0.1 m below the soil surface, unless otherwise specified for other cases studied. The physics regarding heat transfer process within the layers and across interfaces are specified as time dependent accordingly. Note that only the top 10 m of the soil layer is initiated as 100 % water saturated to roughly approximate the reality. The ground cold-water inflow assumes a direction as shown in Figure 7, which may need to be revised as our understanding improves in future. The originate of the coordinate system is setting on the soil surface on the left hand side, as shown in Figure 7.

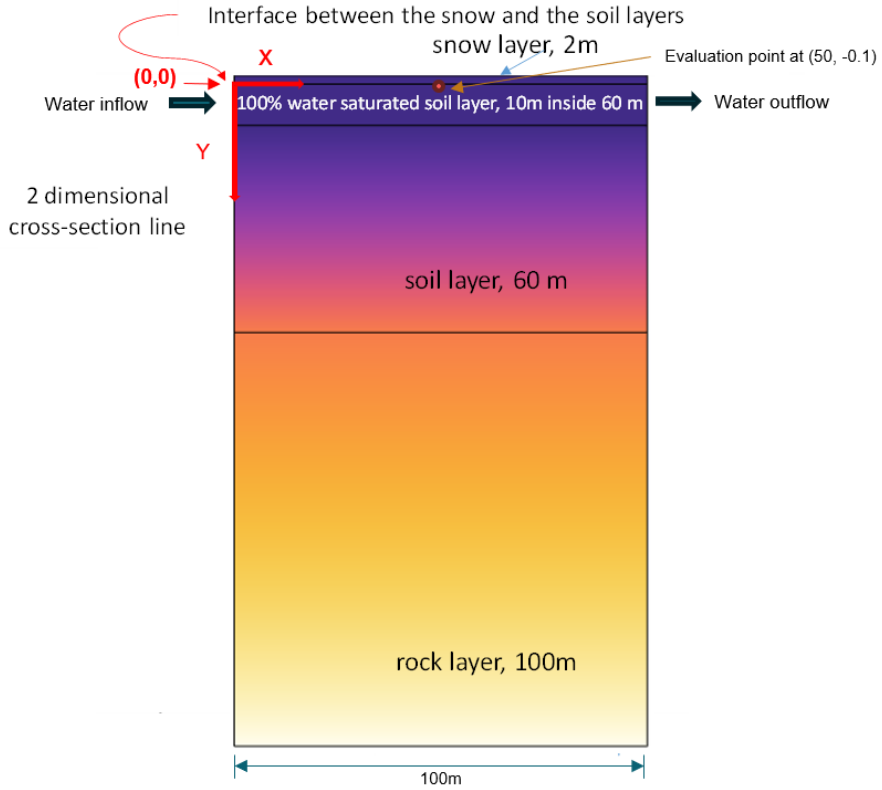

Figure 7: A simplified two-dimensional model for Mount Meager near surface heat transfer process.

More specifically, the geometry of this model is defined as a series of 2D rectangles with an overall dimension of 100m x 162m. There are four main layers in the model shown, they are snow layer, 100% water saturated soil layer, soil layer, and quartz diorite basement from top to bottom. The model is relatively small in geometry because the focus of this study is on the thermal response near the ground soil surface where the sensors locate. In this simulation, the soil layer set from 0m to 60m depth. The soil is defined with a porosity of 0.5, a heat capacity at constant pressure of 2000 J/(kg·K), a density of 1050 kg/m³, and a thermal conductivity of 0.45 W/(m·K). A cold-water at 0 °C, assumed to be snow melted apparently to form ground cold-water flow by underground heat, moves through a 10-meter thick and 100% water saturated soil layer. It enters from the left and exits to the right with various velocity assumed to account for the apparent amount of water generated by snowmelt. Based on temperature dynamics data from the 2020 to 2021 winter period, the initial

soil temperature is set at 2 °C for base case study and for other sensor sites at higher elevations, lower initial soil temperatures can be specified accordingly.

An evaluation point (EP), acting as a sensor location, is placed at a depth of 0.1 m below the soil surface with a coordinate of (50, -0.1), to observe temperature change in the simulation. A ground cold-water flow velocity of 1 x 10^{-4} m/s is assumed for base case study, which is reference to typical aquifer groundwater movement speeds ranging from 0.5 to 50 feet per day (1.8 x 10^{-6} to 1.8 x 10^{-4} m/s) and our preliminary simulation study using COMSOL. During the study, other EPs can be arranged either horizontally or vertically to investigate the effect of sensor location on temperature profile.

The underlying quartz diorite rock occupies the remaining depth of 100 meters. The properties of the quartz diorite include a thermal conductivity of 3.02 W/(m·K), a density of 2860 kg/m³, a heat capacity at constant pressure of 745 J/(kg·K), and a porosity of 0.2. From a depth of 0 m to 160 m, the layers are set to possess a thermal gradient of 0.03 °C /m. Finally, the snow-curtain layer is modeled with a thickness of 2 meters to cover the top of the soil layer. The snow-curtain layer is characterized by a porosity of 0.85, a heat capacity at constant pressure of 2100 J/(kg·K), a density of 917 kg/m³, and a thermal conductivity of 2.1 W/(m·K). The temperature of the snow-curtain layer is set at 0 °C. The parameters for the entire system modeled are summarized in Table 1 below.

Table 1: Parameters applied in the simplified 2D model using COMSOL software.

Parameter	value (unit)
Thermal gradient	0.03 °C/m
Top soil surface temperature	2 °C
Cold water flow temperature	base at 0 °C, and changing
Snow layer temperature	0 °C
Snow thermal conductivity	2.1 W/(m·°C)
Snow density	917 kg/m^3
Snow heat capacity at constant pressure	2100 J/(kg·°C)
Snow porosity	0.85 (fraction)
Soil thermal conductivity	0.45 W/(m·°C)
Soil density	1050 kg/m^3
Soil heat capacity at constant pressure	2000 J/(kg·°C)
Soil porosity	0.5 (fraction)
Quartz diorite thermal conductivity	3.02 W/(m·°C)
Quartz diorite density	2860 kg/m^3
Quartz diorite heat capacity at constant pressure	745 J/(kg·°C)
Quartz diorite porosity	0.2 (fraction)
Fluid velocity	base at 1x10^-4 m/s, and changing
Evaluation point depth	base at 0.1 m, and changing

3. RESULTS AND DISCUSSION

Applying the model built using COMSOL with fine grid scheme, a complete set of simulations has been conducted to study the effects of ground water flow velocity, the initial ground water temperature on temperature profile at the evaluation point (EP). The temperature profiles at different EPs distributed vertically and horizontally with certain ground cold-water velocity have been simulated and presented in this section. From the understanding gain form this study, a number of qualitative matches for the field temperature measurement can be properly achieved with limited field information provided using the COMSOL model built.

3.1 Effect of Ground Cold-Water Flow Velocity

The ground water is assumed to be initiated at the left-hand side of the two dimensional model, shown in **Figure 8**. As indicated in Figures 8a and b, the effect of ground water flow velocity on temperature at the evaluation point (EP) of (50, -0.1) is obvious. Note that Figures 8a and b are the same except for different time durations. Depending on whether the evaluation points (EPs) are flooded by ground water during the simulated time duration of 7 months, the temperature profiles shown in Figure 8 are categorized into two groups: the Group 1 is for the EPs that are flooded or flooded during the later time duration with 7 months, and the Group 2 is for the EPs that are not flooded within 7 months. A careful examination of the simulation results (Figure 8b) indicated that the Group 2 has only one curve which is under the velocity of 1×10^{-6} m/s. The other curves for velocity larger than 1.0×10^{-6} m/s belong to the Group 1.

A general observation for curves in the Group 1 shows that the larger the ground water flow velocity, the more quickly it causes the temperature at the evaluation point (EP) of (50, -0.1) to reach 0 °C, because a faster cold-water flow helps carry away heat more quickly. On the contrary, a slower ground water flow velocity results in a higher temperature at the EP. For example, at the velocity of 1.0×10^{-2} m/s, the temperature at the EP drops to 0 °C within 0.1 months, whereas at the velocity of 5.0×10^{-5} m/s, the temperature drops to 0.77 °C after 0.5 months.

For the outcomes in the Group 2, because the EP is not flooded by the ground water due to the extremely slow ground water velocity and the fact that the EP is located at (50, -0.1), the snow-curtain on ground surface at 0 °C, which prevent geothermal heat from losing into the harsh winter atmosphere, and the conductive geothermal heat transfer become the major heat transmission mechanisms. These mechanisms generate the temperature profile shown in the Group 2, which increases dynamically over time within 7 months. For a much longer simulation duration after 7 months under the same simulation conditions, our theoretical study indicated that the temperature profile will eventually decreases dynamically due to heat loss; however, given the cyclic seasonal weather pattern of earth atmosphere and the changing trend presented in the field data collected, simulation outcomes for any duration longer than 7 months are not directly related to the actual field temperature data and therefore are not presented in this article.

Another clear observation is that during the initial 0.1 months, all temperature profiles experience a dramatic drop at the EP, due to the covering of ground soil surface by the falling 0 °C cold snow. After this early period, a dynamic thermally balanced temperature profile is temporarily attained at around 0.8 °C. Over the next 4 months, the gradual heating of the soil layer by the underground geothermal heat contributes to a gradual increase in temperature.

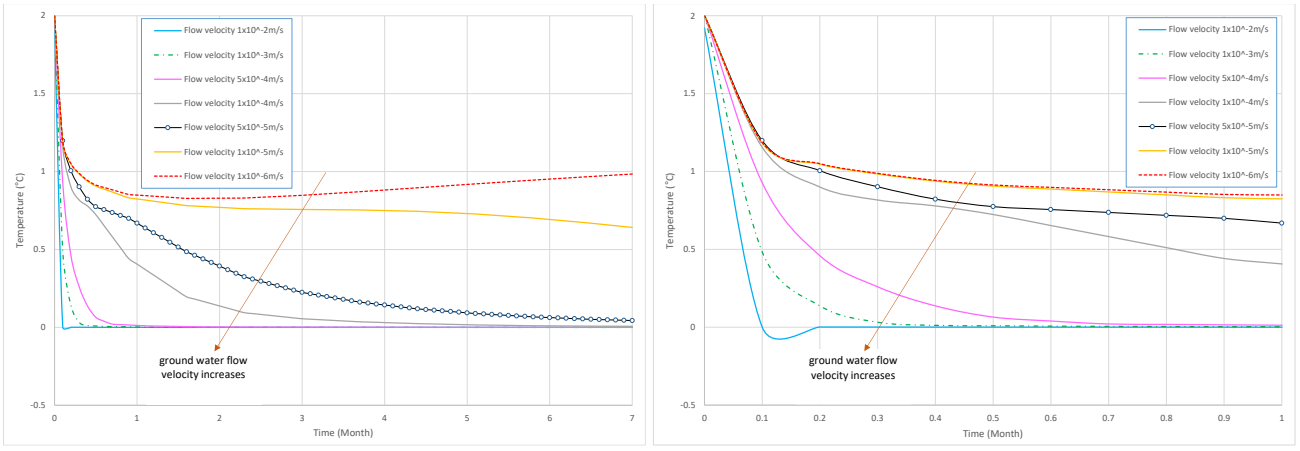

Figure 8: The effect of ground water flow velocity on the temperature at EP (50, -0.1). (a) for a duration of 7 months, and (b) for the first month duration.

3.2 Effect of Ground Cold-Water Temperature

In order to investigate the effect of the temperature of the ground water flowing with a velocity of 1×10^{-4} m/s and injected into the model at the left-hand side of the model as before, the initial ground water temperature was investigated under 0 °C, 0.5 °C and 1.0 °C. The simulation outcomes presented in **Figure 9** show that before the ground cold-water arrives the EP at the end of day 3 (this time point is

evaluated from Figure 8b accordingly), the 0 °C cold snow reduces the temperature at the EP from 2 °C to 1.15 °C. After the end of day 3, the temperature profile changes accordingly depending on the initial temperature of the ground cold-water and its heat balance with the subsurface conductive geothermal heat. The duration between day 3 and day 6 is a transitional for all cases simulated. The temperature profiles gradually stabilized as time proceeds. In general, the higher the temperature of the ground cold-water flow, the higher the temperature value at the EP location. This is physically meaningful and correct.

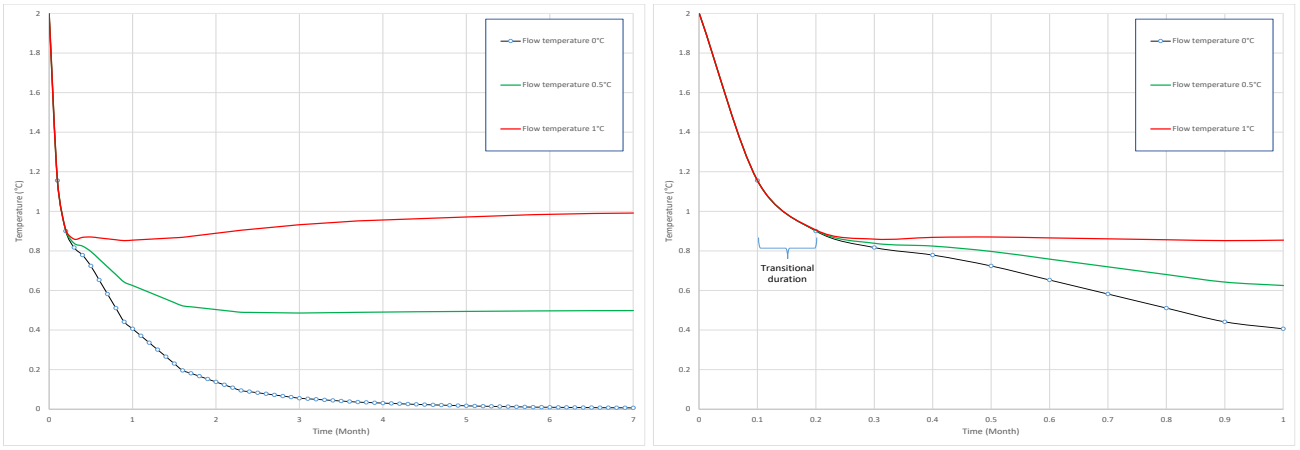

(a) (b)

Figure 9: **The effect of initial ground water temperature on temperature profile at the EP of (50, -0.1) with ground water velocity of 1 x 10^{-4} m/s. (a) for a duration of 7 months, and (b) for the first month duration.**

3.3 Effect of Evaluation Point Depth

Figure 10a presents the influence of the depth of the evaluation point (EP) where a postulated temperature sensor is placed, under the assumed ground water velocity of 1 x 10^{-4} m/s and the other parameters listed in Table 1. It is observable from this figure that as the EP depth increases the temperature profile becomes higher in general. In another word, deeper EPs exhibit higher temperature profiles, and the whole system takes a longer time for the 0 °C ground water flow to help cool down the temperature in subsurface layers. It is concluded that the combined dynamic influence of the geothermal heat transfer from deeper subsurface to EP and the heat loss through 0 °C ground water flow at EP jointly contribute to the gradual decrease of the temperature profile. This highlights the influence of EP depth in this process.

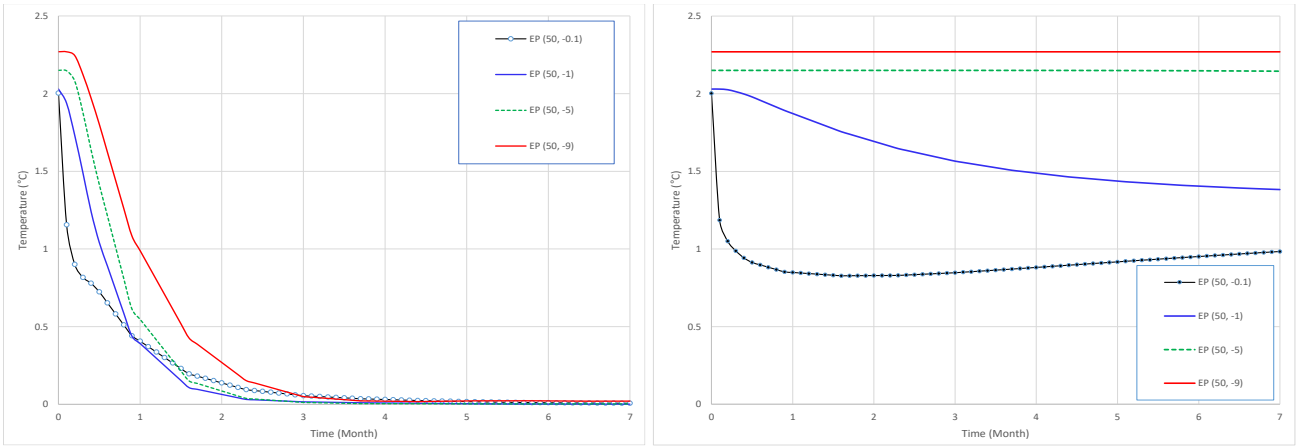

(a) (b)

Figure 10: The temperature profiles simulated at different evaluation depths with different ground cold-water velocities. (a) for flow velocity of 1 x 10^{-4} m/s, and (b) for flow velocity of 1 x 10^{-6} m/s.

Figure 10b shows the temperature profiles at different EPs with ground cold-water velocity of 1 x 10^{-6} m/s, and the other parameters remain the same as listed in Table 1. At a first glance, Figure 10a and b are quite different. This is caused by the large difference existed in ground water flow velocity. With the slower ground cold-water velocity of 1 x 10^{-6} m/s, the EPs at (50, -5) and (50, -9) do not meet the ground water front within 7 months. Therefore, their temperature profiles remain affected by the original geothermal status only, which is stabilized normally.

For the shallower EPs at (50, -0.1) and (50, -1) the physics are different. At EP (50, -0.1), the assumed 2 °C soil surface is initially covered by the 0 °C snow-curtain layer. Initially, the dynamic heat transfer process causes a rapid temperature drop to nearly 1 °C. After reaching this point, the temperature decreases more slowly. When the temperature reaches 0.8 °C around 2 months, a dynamic balance is achieved between the geothermal heat from the bottom and the 0 °C snow-curtain layer from the top, resulting in an equilibrium state. The temperature then remains around 0.8 °C for nearly a month. Subsequently, the temperature increases very slowly due to the influence of underground geothermal heat. This observation provides insight into the dynamic thermal processes within the soil under snow-curtain when the external ground cold-water flow is not present. At EP (50, -1), the thermal impact of the 0 °C snow-curtain layer is less pronounced, compared to its effect on the shallower EP at (50, -0.1). As a result, the temperature at (50, -1) EP drops more gently over time. It stabilizes once it reaches the early time equilibrium temperature, and further temperature reduction is much limited due to geothermal heat support underneath.

3.4 Temperature Profiles Simulated at Different EPs in Horizontal Direction

The temperature profiles at three different EPs, i.e., points of (25, -0.1), (50, -0.1) and (75, -0.1), along the horizontal direction are evaluated under the same assumed ground water velocity of 1 x 10^{-4} m/s and the other parameters listed in Table 1. Similar to early cases studied, the sudden temperature drop during the very early time (< 0.1 months) is caused by the 0 °C top snow-curtain. Physically, the (25, -0.1) position meets the 0 °C ground cold-water earlier and has the longest exposure duration to the continuous cold-water flow which helps carry away the conductive geothermal heat transferred to the position, thus the temperature profile at this point is the lowest. While the (75, -0.1) position meets the ground water much later at roughly day 12, and the ground water at this position and time may also has been slightly heated up by the environment as indicated by the flat temperature plateau between day 3 and day 12. Therefore, the temperature profile at this location (75, -0.1) is much higher as indicated in **Figure 11**. As time proceeds, the temperatures at all EPs are approaching 0 °C gradually due to the systematic dynamic heat balance between the cold temperature ground water flow in the topsoil layer and the conductive geothermal heat transfer from the bottom rock layer.

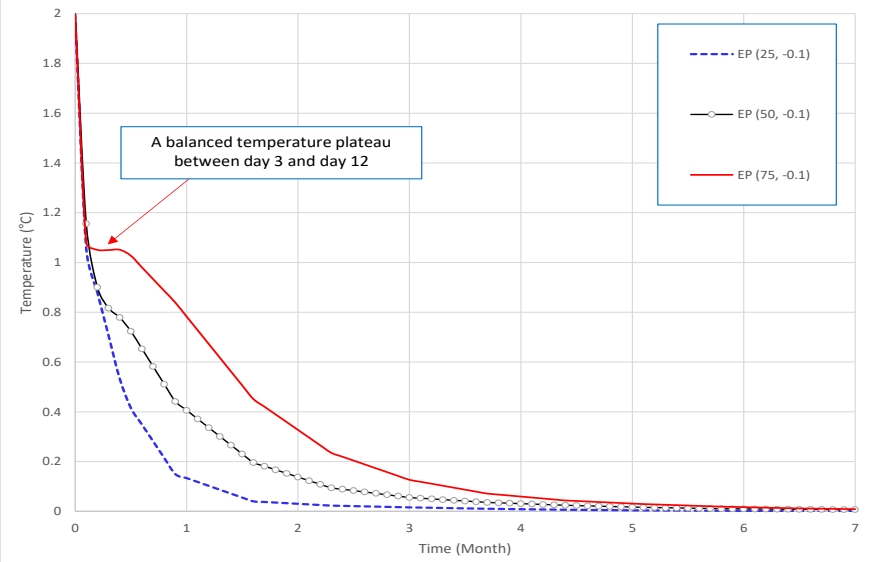

Figure 11: The temperature profiles simulated at different EPs along horizontal direction, ground water velocity of 1 x 10^{-4} m/s.

3.5 Qualitative Matching of Field Temperature Measurement

For this qualitative study, we would like to see a temperature profile roughly close to the field data based on the available limited field information. One can observe in **Figure 8** that when the flow velocity assumes 1 x 10^{-4} m/s, a proper matching result and correct temperature data trend are generated under the other conditions listed in Table 1. The outcomes in Figure 8 show that, in the initial 3 days, the temperature drops from 2 °C to 1.2 °C due to the influence of cold snow on the ground soil surface. After 6 days, once the ground water reaches the evaluation point, the temperature starts to decrease gradually due to the effects of the flowing cold-water and reaches 0 °C at 5 months and stays near 0 °C eventually. Given the uncertainty in parameters and even our incomplete understanding of the working mechanisms for this process, the outcomes can be regarded as satisfactory. Therefore, a ground water flow velocity of 1 x 10^{-4} m/s is chosen to perform qualitative study for the following simulated cases. In reality, because ground water flow velocity varies with time and space and is affected by many factors it is challenging to capture velocity information accurately for field cases. Therefore the study provided here under fixed velocity is of reference value and the research conducted is qualitative in nature.

Based on the studies conducted, it is realized that the overall qualitative matching outcomes for all of the three categories of field temperature time series can be roughly matched by adjusting the ground cold-water velocity and its initial temperature, the temperature of snow-curtain, the position of EP horizontally and vertically, and the other corresponding parameters listed in Table 1. For example, by assuming the ground water flow velocity of 1 x 10^{-4}m/s and setting the its temperature to 0.2 °C, with the other parameters remain as

listed in Table 1, one can also qualitatively match the temperature time series in the Category 2, which is the moderate temperature zone curve as shown in **Figure 12b.** In order to qualitatively match the temperature time series in the Category 1, which is the high temperature zone, one may shift the evaluation point horizontally from 50 m to 95 m to match the curves within Category 1, as shown in **Figure 12a.** Clearly, for Category 3 curves with low temperature time series, the main contributing factors are: higher ground cold-water velocity and its lower initial temperature, lower temperature of snow-curtain, shallower EP position and earlier exposure to the ground cold-water flow. The temperature time series in this Category 3 needs to be studied further due to the complexity.

The typical reasonable matching results achieved and presented in Figure 12 for the Categories 1 and 2 can be regarded as satisfactory because of the current limited availability of true field data and the complexity of the natural phenomena involved. The research in this area may need to be continued in future.

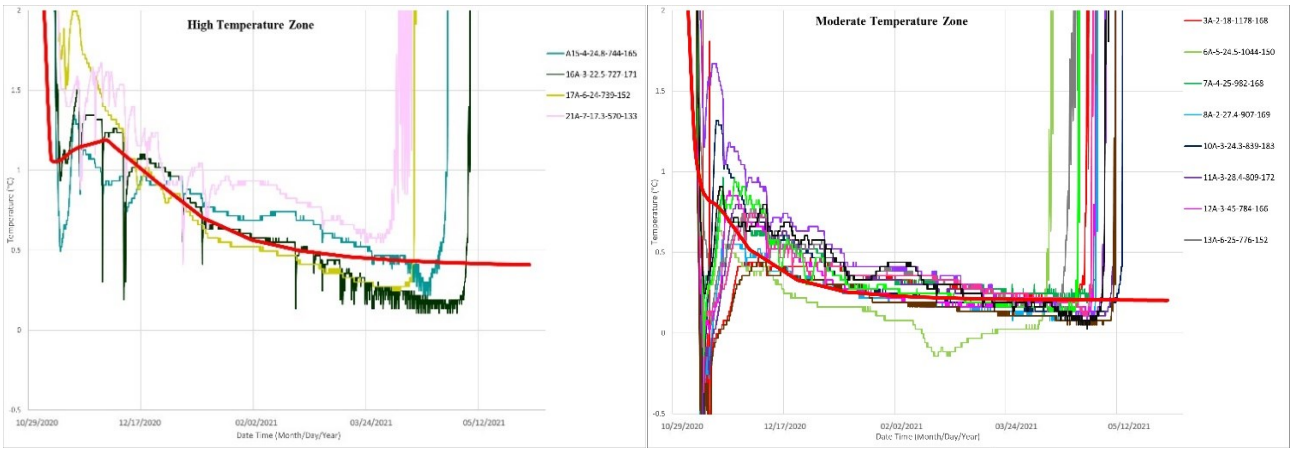

(a) (b)

Figure 12: Qualitative matching for the Categories 1 and 2 field temperature measurement using COMSOL 2D model built.

4. PRESENTATION OF MEASURED DATA USING GEOSTATISTICS TECHNIQUES

This study applies the geostatistical estimation algorithms of Simple and Ordinary Kriging (SK and OK) to generate the estimated temperature at various consecutive time points to help reveal the temporal temperature variation of the Mount Meager geothermal field. Because of the difficulty in clearly identifying the key information from the complicated temperature dataset, the application of geostatistical techniques and algorithms can be helpful.

4.1 Data Organization

The measured data in the snow-curtain period are organized using equal spaced data recording points to represent the temporal variation of the ground temperature dynamics. Eight time points were designed to represents the snow-curtain period, namely TP1 to TP8. First seven are equal spaced. TP1 is at the beginning of the snow-curtain period, the number of time points increases followed as time goes on, and TP7 is near the end of the snow-curtain period: TP1(4500), TP2(5500), TP3(6500), TP4(7500), TP5(8500), TP6(9500) and TP7(10500). TP8(10900) is added to the very end of the snow-curtain period where the number in the round brackets indicated the n^{th} temperature records in the data matrix. The positions of the sensors in latitude and longitude in degree unit are applied (Universal Transverse Mercator (UTM) system can be used too) to compute the lag distance, and then the histogram of the lag distances among all of the sensor positions is shown in **Figure 13**. The mean value is 0.02917 and the variance is 0.000474129, these parameters is essential in the variogram modeling process, because in a variogram, the degree of discontinuity of a variable is determined by direction and lag distance (Cao et al., 2014).

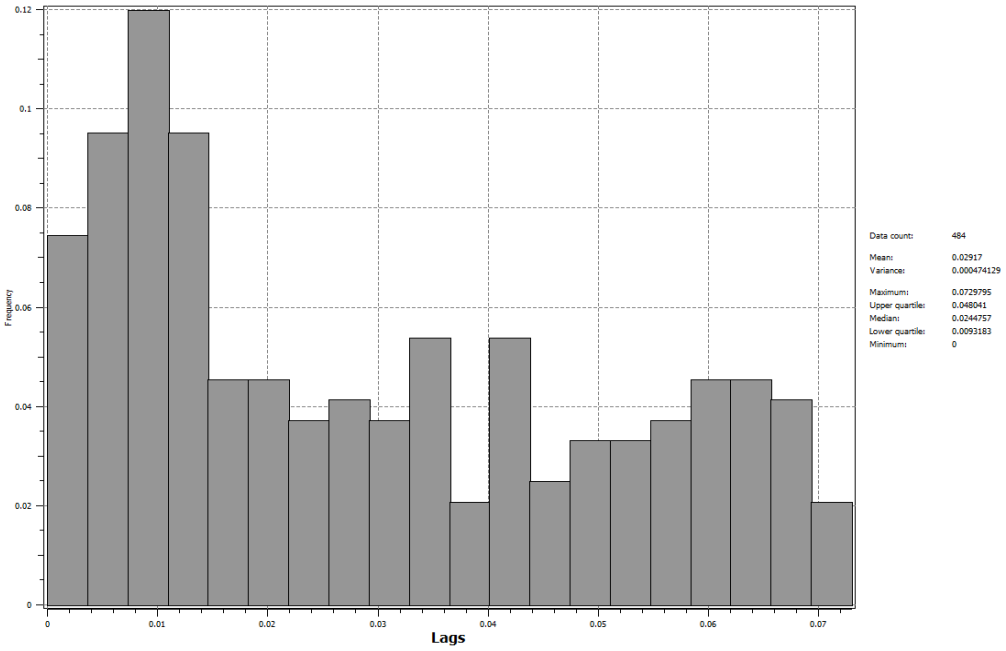

Figure 13: The histogram of the lag distances among all sensor positions.

4.2 Data Presented Using SK and OK Estimation

The statistics of these seven time points, their isotropy variogram models, and the SK and OK estimates of temperature are shown in the Figures of A1 to A8 in Appendix A. In the estimation process, the sampled data variance, which can be read from histogram, is used for variogram modeling and the ranges were adjusted to generate a proper match. The mean value of sampled data also is roughly estimated from histogram, which is an important parameter used in Simple Kriging. In the variogram modeling, the variances of sampled data at some time points are lower than the sill values captured by the calculated variogram. This may be caused by the insufficient sample data and the calculated variogram may have actually secured some structural relationship among the data. For example, it is likely that hole effect exists among the sampled temperature data as shown in the variogram modeling figures presented in Appendix A, which may need further study in future (Kelkar et al., 2002; Pyrcz and Deutsch 2003). This requires that the calculated sill value needs to be modeled and used. However, because this consideration does not strongly support by the limited data at this moment, a conservative approach was taken, which uses the variance of the sampled data as the targeted sill value in modeling. In this study, isotropy variogram modeling is conducted for simplicity. The modeling outcomes at several representative temporal points are chosen to present, namely at TP1, TP2, TP7, and TP8.

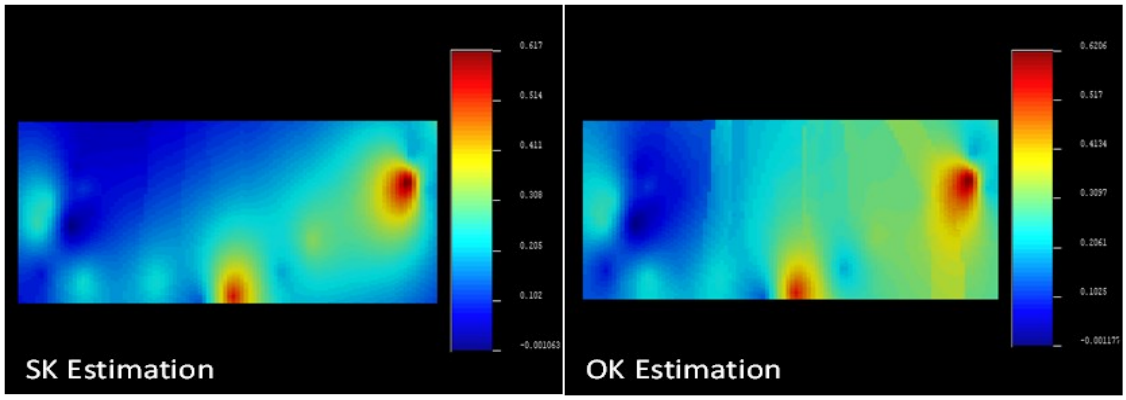

(a)

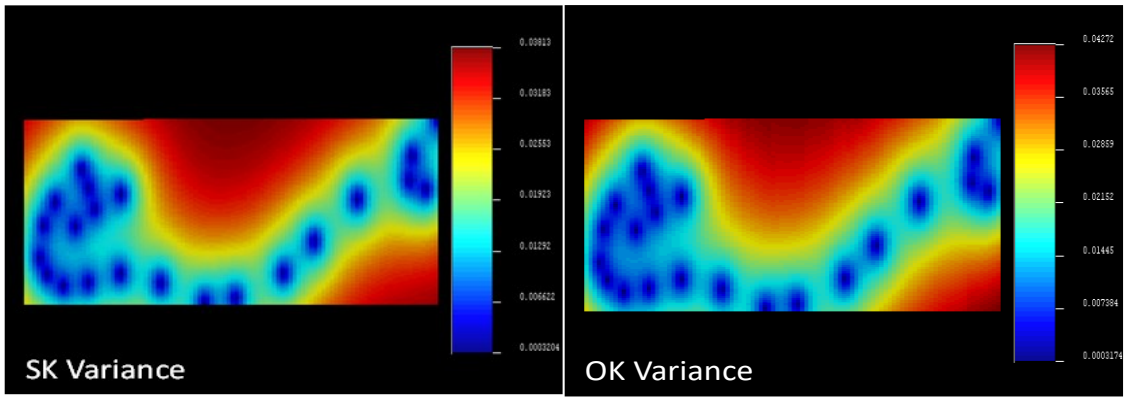

(b)

Figure 14: The temperature estimated using SK and OK methods (a) with their estimation variances (b) of TP1(4500).

TP1 is the first time point of our investigation, that is, at the beginning of the snow-curtain period. The mean value of TP1 dataset is 0.213091. The variance is 0.0242729, which is a measure of dispersion. A smaller value of variance indicates more consolidation in the sample dataset. The isotropy variogram model with a sill value of 0.1, the maximum range of 0.04, and the minimum range of 0.03. Both the maximum range and minimum range are in degree. The parameters presented above could easily captured from Figure A1 (a) and (b) in Appendix A. Also, these values have also been used in Simple Kriging and Ordinary Kriging methods to model the temperature mappings. Figure 14a shows the temperature mappings estimated through Simple Kriging method and Ordinary Kriging method. Both methods yield comparable temperature mappings. Figure 14b displays the variance profiles computed from the Simple Kriging method and Ordinary Kriging method. These illustrations effectively demonstrate the sensors' locations, as those areas have lower variances. Conversely, as the distances between the sensors increases, the variances become larger.

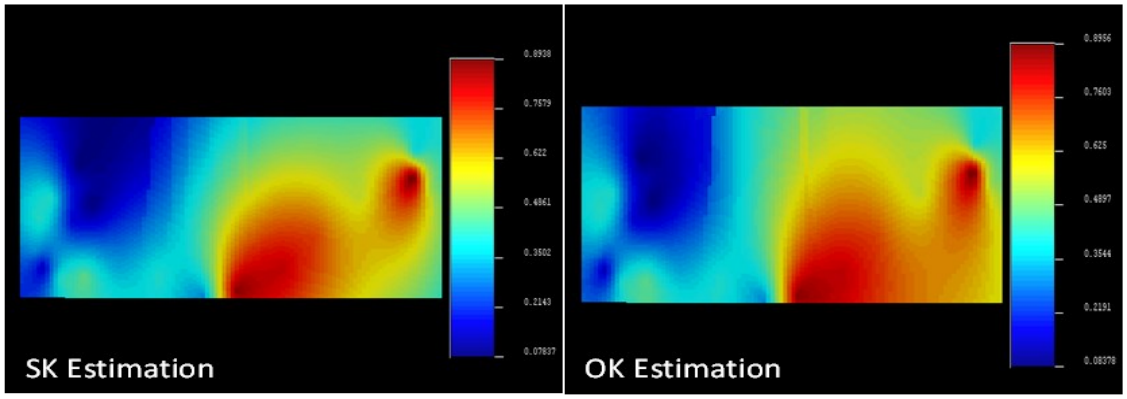

(a)

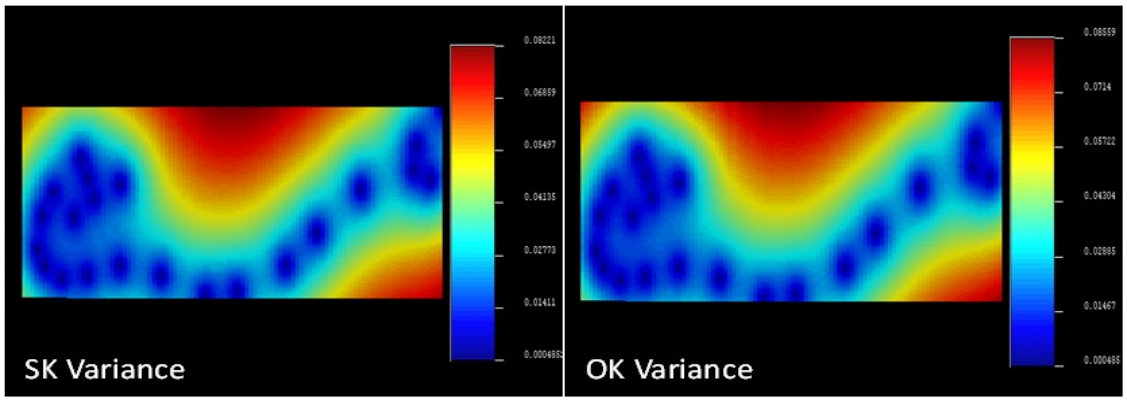

(b)

Figure 15: The temperature estimated using SK and OK methods (a) with their estimation variances (b) of TP2(5500).

The temperature mappings and variance profiles at TP2 are shown in Figure 15a and b. A detailed comparison between TP1 and TP2 reveals a similar temperature distribution, with temperature increasing as time passes, similar to the observed trend of temp erature between TP1 and TP2.

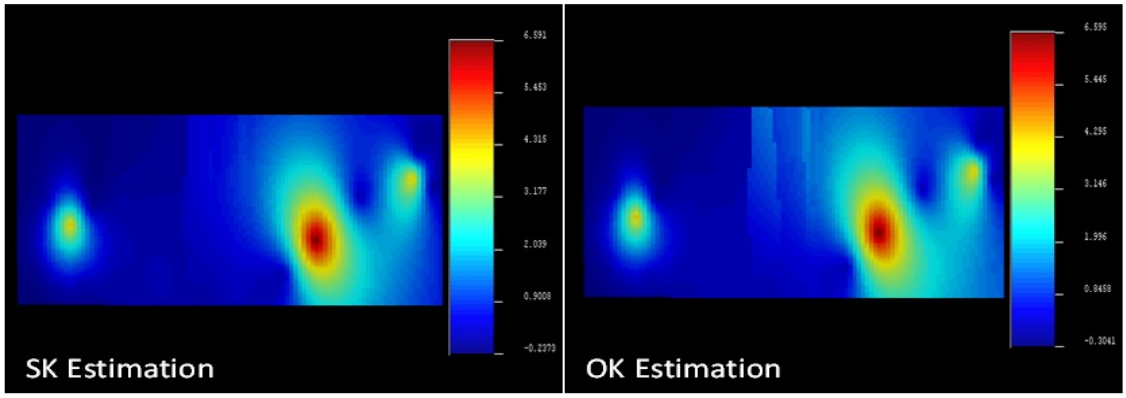

(a)

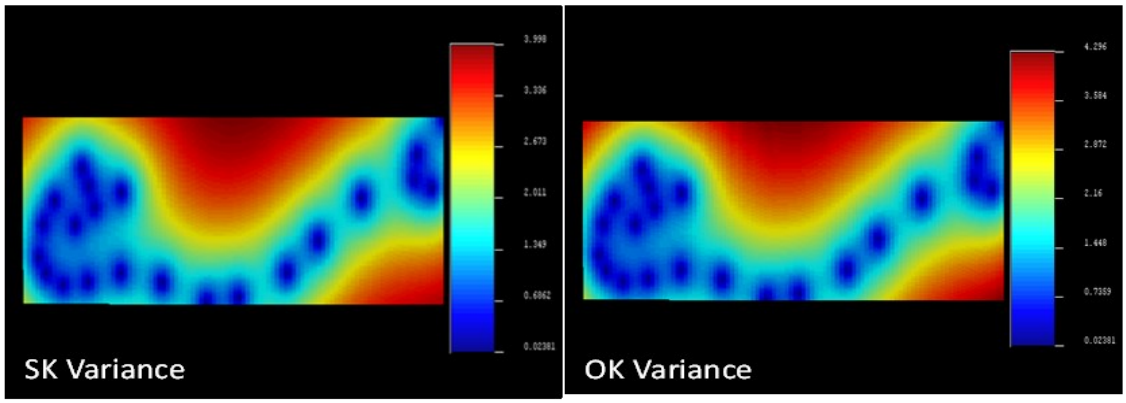

(b)

Figure 16: The temperature estimated using SK and OK methods (a) with their estimation variances (b) of TP7(10500).

At TP7 three heat sources can be easily found, as shown in **Figure 16**a. Two heat sources on the right hand side of the temperature mapping are near the Meager Creek Fault and the rightmost point is at the Meager Creek Hot Spring compared with the Google satellite map. There is also a light heat source at the top of the mountain and near the No Good Creek Fault. TP7 is the end point of the snow-curtain period; most of the snow has melted due to the rising temperature. So, only the heat sources with higher temperatures could be seen in the temperature mapping. By comparing the temperature mapping with those of the previous temporal points, the temperature is higher than others and conforms to the actual temperature data collected.

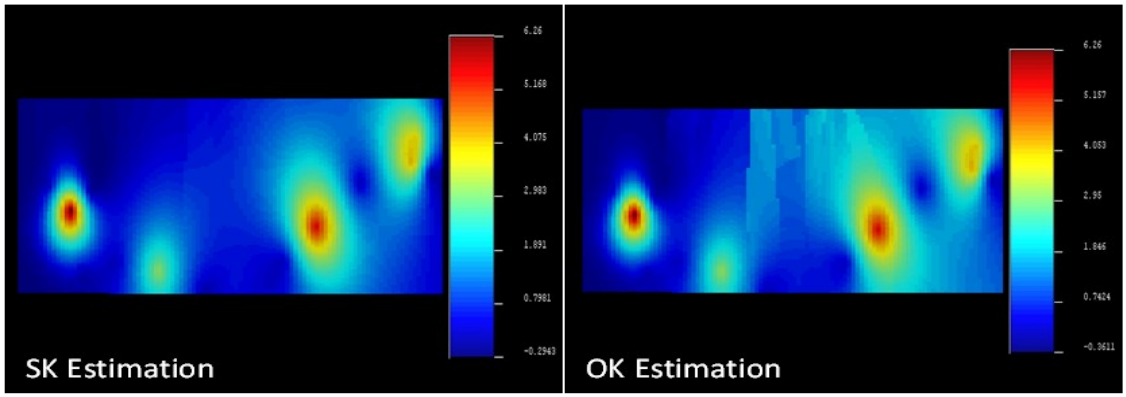

(a)

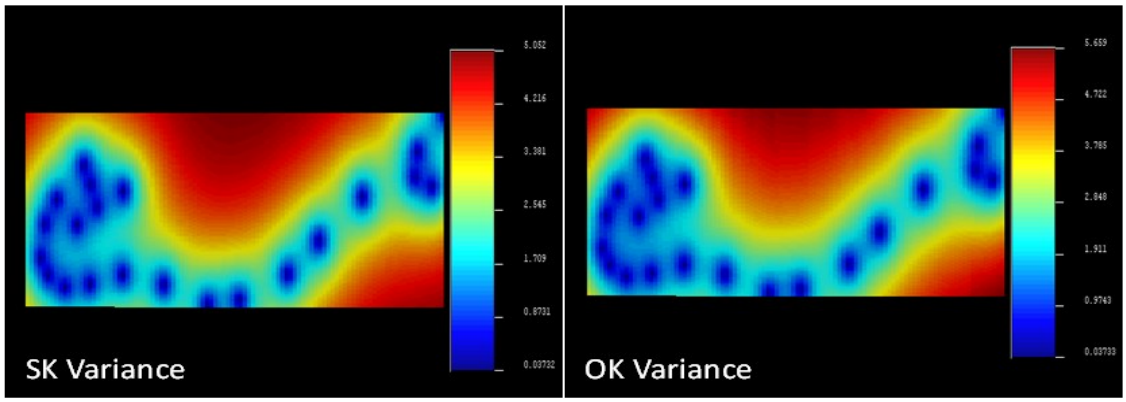

(b)

Figure 17: The temperature estimated using SK and OK methods (a) with their estimation variances (b) of TP8(10900).

Using SK and OK methods, one more light heat source at TP8 has been identified in **Figure 17**a compared with mapping of the TP7. This heat source is at the left hand side bottom of the mountain and near the No Good Creek Fault. At TP8, the sensors were likely under snow-curtain with reduced snow thickness (near the end of the winter) and detected the heat transfer from the underground heat sources as time passed. This is the reason why we add one more time point to investigate the temperature mapping. Therefore, a total of four heat sources have been discovered within the surveyed area.

5. CONCLUSION

The following conclusions can be drawn from this preliminary study:

1. The temperature sensor data from the Mount Meager area can be characterized into three categories as presented accordingly, depending on the range of the measured temperature and the trends of changing.

2. The categorization of the temperature curves into three groups in terms of high, moderate and low temperature zones is meaningful. The results from the 2D numerical simulation are valuable, providing insights for data interpretation. The high temperature curves are near the surface geothermal heat sources (hot springs), the moderate curves are likely recoded in the areas with relatively larger ground water flow around the alluvial fan area near the foot of the Mount Meager, and the low temperature curves are at sites with higher elevation where ground water is colder.

3. The Simple and Ordinary Kriging (SK and OK) were applied to generate temperature maps at various consecutive temporal points to reveal the temporal dynamic temperature variation of the Mount Meager geothermal field. The preliminary results in this study suggest that our general understanding based on the categorization of the sampled data is consistent with the insights revealed through temporal temperature field mapping by geostatistics.

4. The heat sources hidden underneath the snow-curtain can be clearly identified through temporal temperature mapping using geostatistical methods. Careful simulation of hole effect by applying zonal anisotropic variogram modeling may further help identify subtle heat sources from the field dataset. The results presented in this geostatistical study help reveal the significance of how underground heat sources, hot springs, and snowmelt affect the temperature profiles at different EPs.

5. Currently a general understanding and qualitative evaluation of the sampled data are achieved. A simplified preliminary qualitative numerical study using COMSOL multiphysics software has been conducted through building a two-dimensional model with idealized geothermal heat source and parameter setting to help identify the heat flux range and the temperature distribution of the targeted area.

6. Based on the qualitative studies conducted through using COMSOL multiphysics software, it is realized that the field temperature time series can be roughly matched by mainly adjusting the ground cold-water velocity and its initial temperature, the temperature of snow-curtain, the position of EP horizontally and vertically, and the other corresponding system parameters listed.

7. The typical reasonable matching results achieved and presented can be regarded as satisfactory because of the current limited availability of true field information and the complexity of the integrative natural phenomena involved. The research in this area may need to continue in future. The recommendation for future research is to build an accurate multiphysics model that can simultaneously consider the snow accumulating and melting processes under more realistic conditions.

ACKNOWLEDGEMENT

The authors would like to thank the Geological Survey of Canada – Calgary for setting up this research project with funding support to the University of Regina. The field data offered and the invaluable technical communication conducted throughout the research process are highly appreciated. Technical support from COMSOL multiphysics software is acknowledged.

REFERENCE

Agnihotri, J., and Coulibaly, P. (2020). Evaluation of Snowmelt Estimation Techniques for Enhanced Spring Peak Flow Prediction. Water 12, no. 5: 1290. https://doi.org/10.3390/w12051290.

Cao, R., Zee Ma, Y., & Gomez, E. (2014). "Geostatistical Applications in Petroleum Reservoir Modelling." Journal of the Southern African Institute of Mining and Metallurgy, Volume 114, no.8: 625–31. ISSN: 2411-9714.

Chen, Z., Stephen E, G., Yuan, W., & Liu, X. (2023). "Ground Surface Temperature Monitoring Data Analysis and Applications to Geothermal Exploration in Volcanic Areas, Mount Meager, Western Canada." Geothermics, Volume 108. https://doi.org/10.1016/j.geothermics.2022.102610.

Geoscience BC. Mount Meager geothermal data compilation project. Project code: 2017-006, (2017).

Harter, T. (2003). Basic concepts of groundwater hydrology, ISBN-13: 978-1-60107-258-0, DOI: 10.3733/ucanr.8083.

Kelkar, M., Perez, G., & Chopra, A. (2002). Applied Geostatistics for Reservoir Characterization. Society of Petroleum Engineers Richardson, TX. ISBN: 978-1-61399-931-8, https://doi.org/10.2118/9781555630959.

Kitanidis, P, K. (1997). Introduction to Geostatistics: Applications in Hydrogeology. Cambridge university press. ISBN: 0-521-58747-6.

Krige, D, G. (1951). A Statistical Approach to Some Basic Mine Valuation Problems on the Witwatersrand. Journal of the Southern African Institute of Mining and Metallurgy. Volume 52, no.6: 119–39. https://hdl.handle.net/10520/AJA0038223X_4792.

Matheron, G. (1963). Principles of Geostatistics. Economic geology. Volume 58, no:8: 1246–66. https://doi.org/10.2113/gsecongeo.58.8.1246.

Oliver, M.A. (1987). Geostatistics and Its Application to Soil Science. Soil use and management Volume: 3, no:1: 8–20. https://doi.org/10.1111/j.1475-2743.

Oliver, M. A. (2010). Geostatistical Applications for Precision Agriculture. Springer Science & Business Media. ISBN: 978-90-481-9132-1.

Pyrcz, M. J., & Deutsh, C.V. (2003). The Whole Story on the Hole Effect. Geostatistical Association of Australasia, Newsletter 18: 3–5.

Renard, P., Demougeot-Renard, H., & Froidevaux, R. (2005). Geostatistics for Environmental Applications. ISBN: 978-3-540-26533-7. https://doi.org/10.1007/b137753.

Singh, P., Gan, T. Y., & Gobena, A.K. (2009). Evaluating a Hierarchy of Snowmelt Models at a Watershed in the Canadian Prairies. Journal of Geophysical Research: Atmospheres, Vol 114, D04109. https://doi.org/10.1029/2008JD010597.

Vidal, A., and Archer, R. (2015). Geostatistical Simulations of Geothermal Reservoirs: Two-and Multiple-Point Statistic Models. In Proceedings World Geothermal Congress. Melbourne, Australia, April 19-25, 2015.

Witter, J. B, Trainor-Guitton, W. J., & Siler, D. L. (2019). Uncertainty and Risk Evaluation during the Exploration Stage of Geothermal Development: A Review. Geothermics, Volume 78: 233–42. https://doi.org/10.1016/j.geothermics.

Appendix A

The modeling outcomes using geostatistics techniques for multiple TP points in time are presented here for reference purpose.

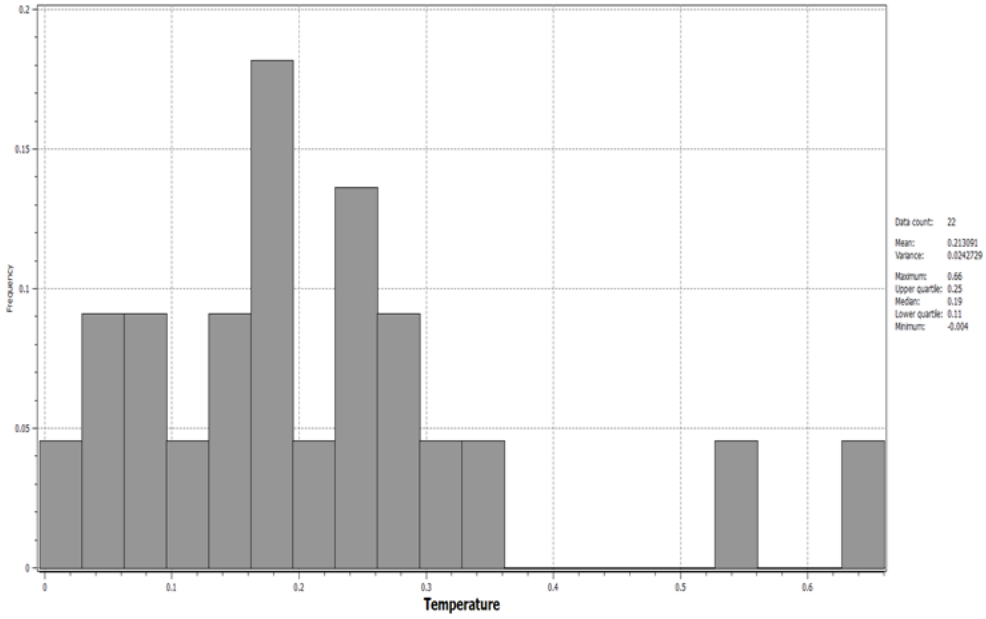

(a)

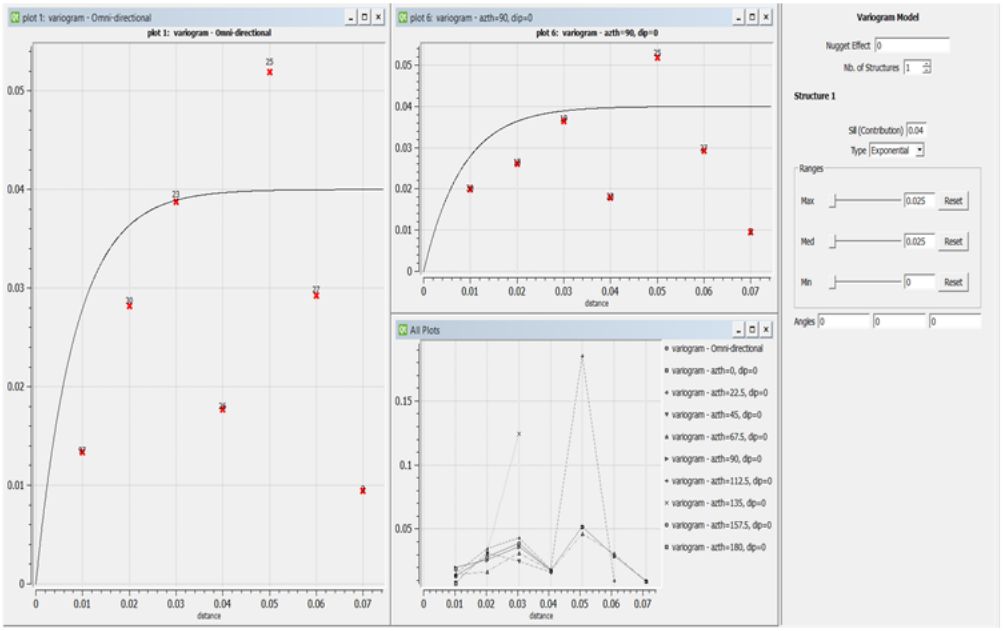

(b)

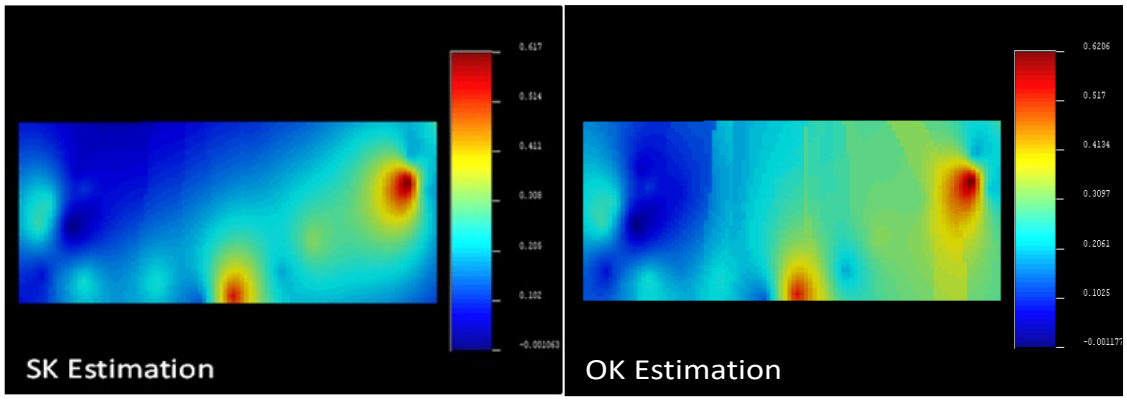

(c)

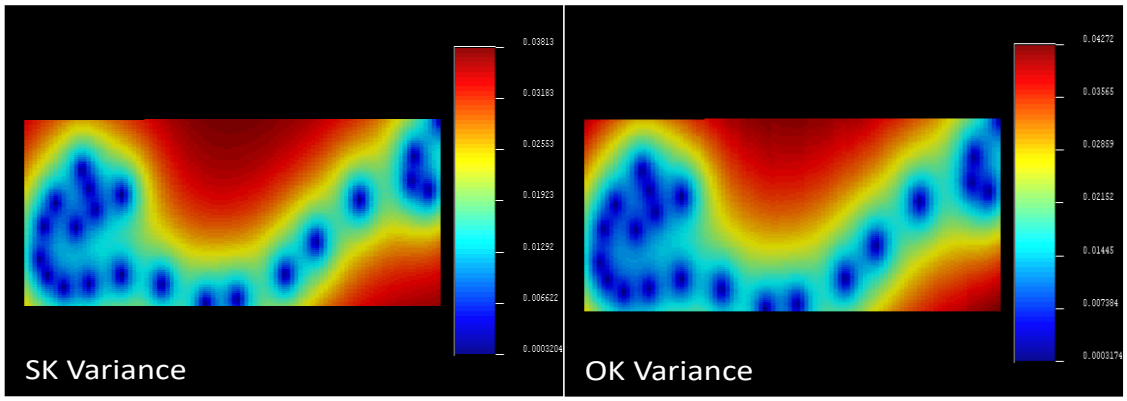

(d)

Figure A1: The statistics of TP1(4500) (a), its isotropy variogram model (b), and the temperature estimated using SK and OK methods (c), with their estimation variances (d).

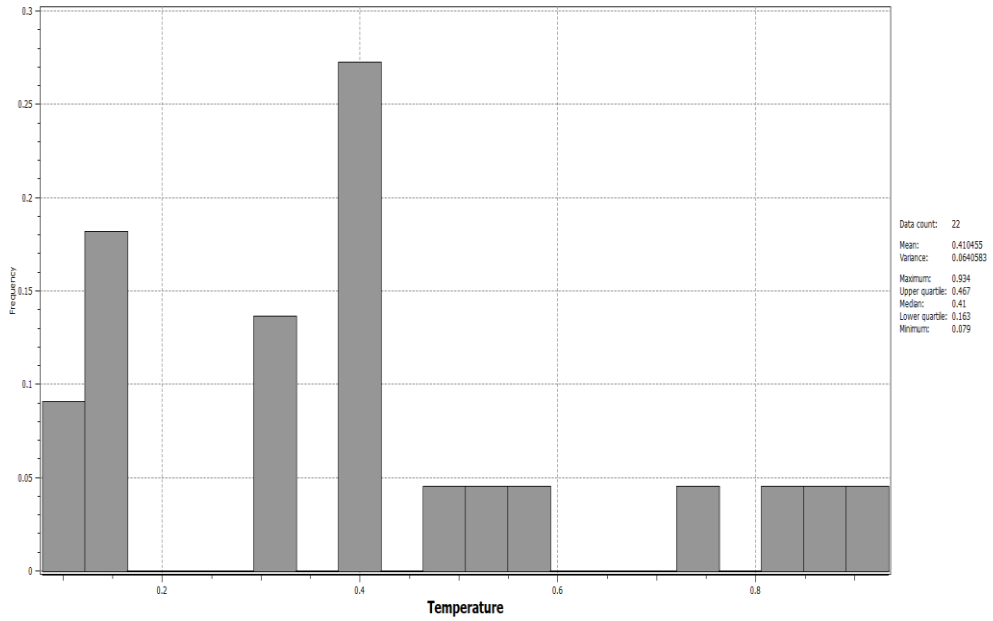

(a)

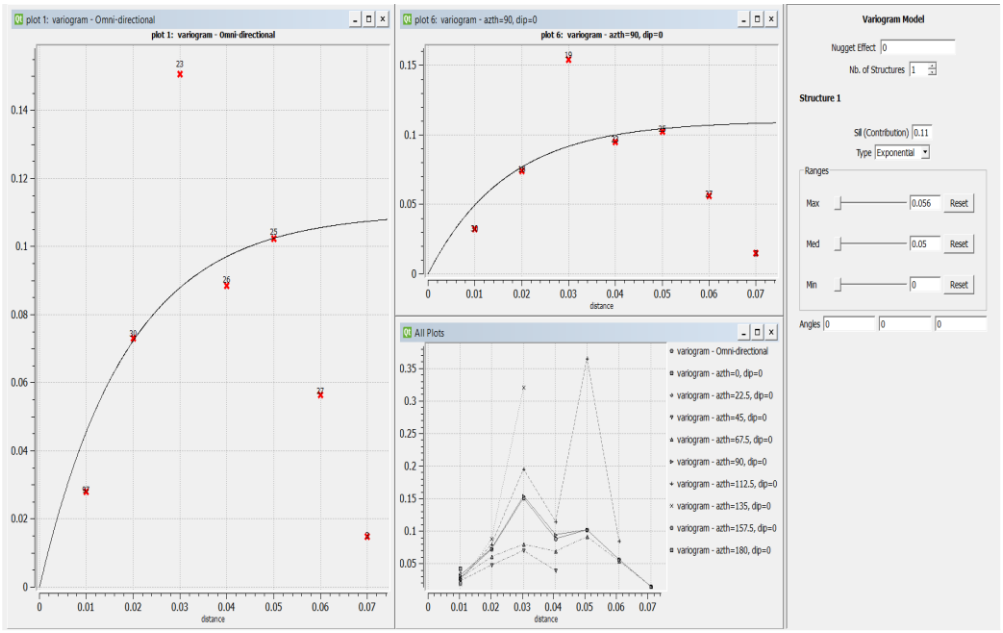

(b)

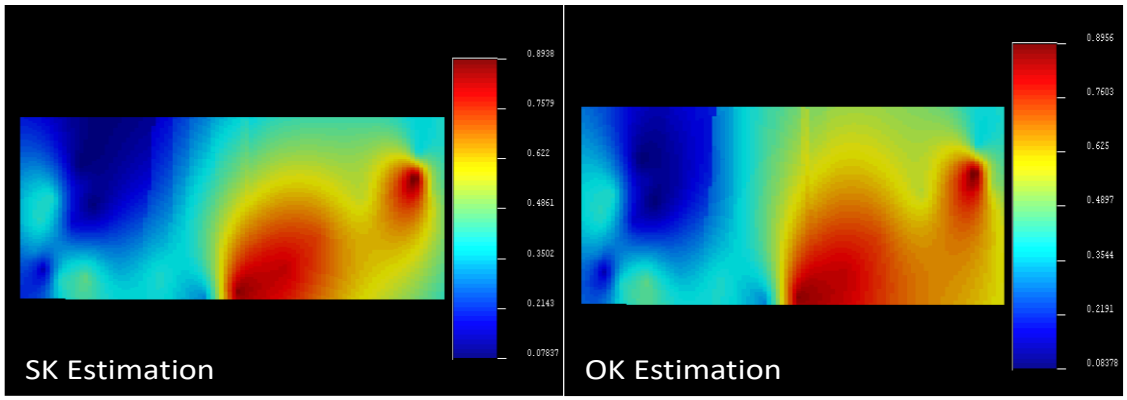

(c)

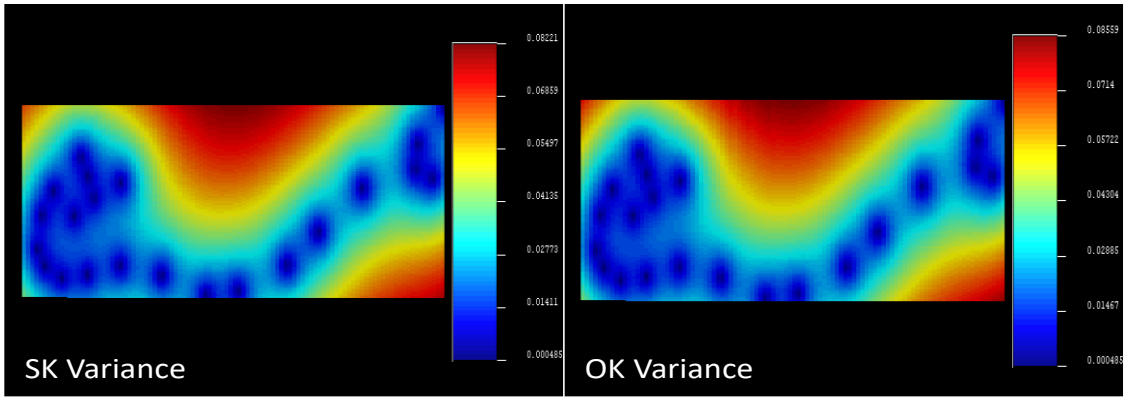

(d)

Figure A2: The statistics of TP2(5500) (a), its isotropy variogram model (b), and the temperature estimated using SK and OK methods (c), with their estimation variances (d).

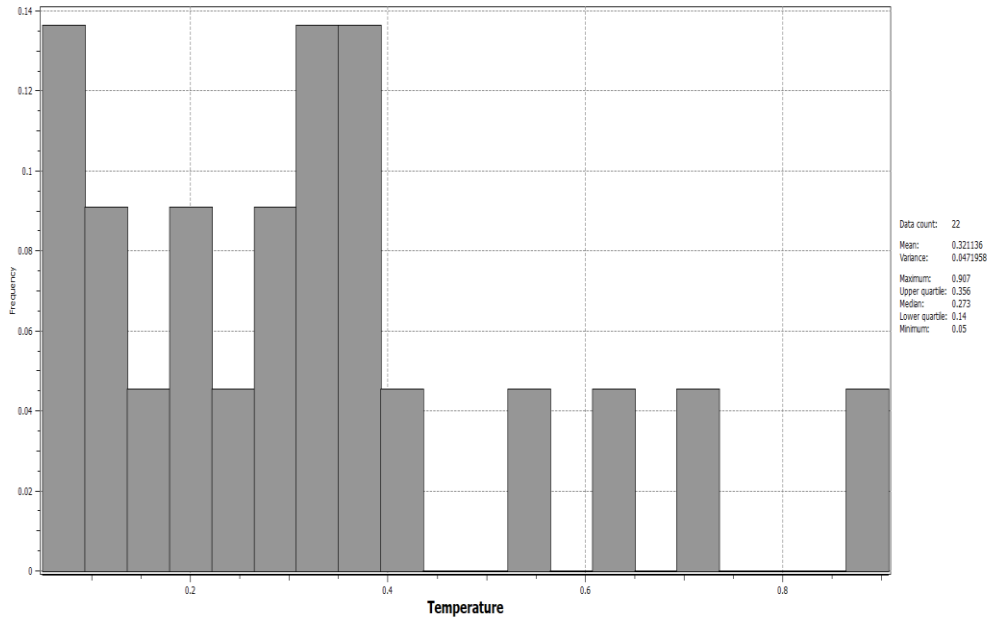
Frequency
Temperature
Data count: 22
Mean: 0.321136
Variance: 0.0471958
Maximum: 0.907
Upper quartile: 0.356
Median: 0.273
Lower quartile: 0.14
Minimum: 0.05

(a)

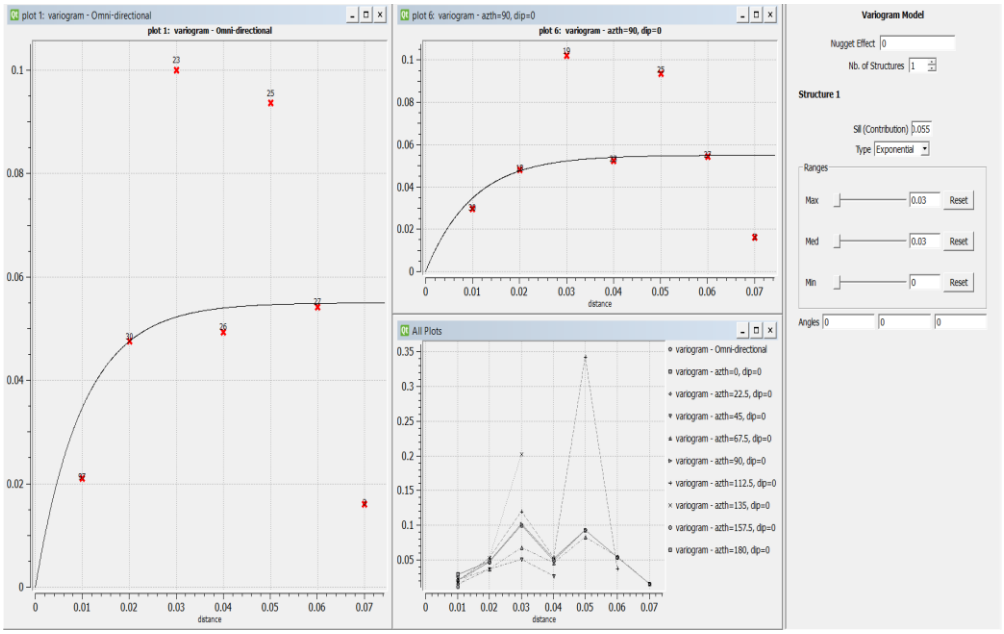
plot 1: variogram - Omni-directional
plot 6: variogram - azth=90, dip=0
All Plots
Variogram Model
Nugget Effect
Nb. of Structures
Structure 1
Sill (Contribution)
Type
Exponential
Ranges
Max
Med
Min
Reset
Angles
distance

(b)

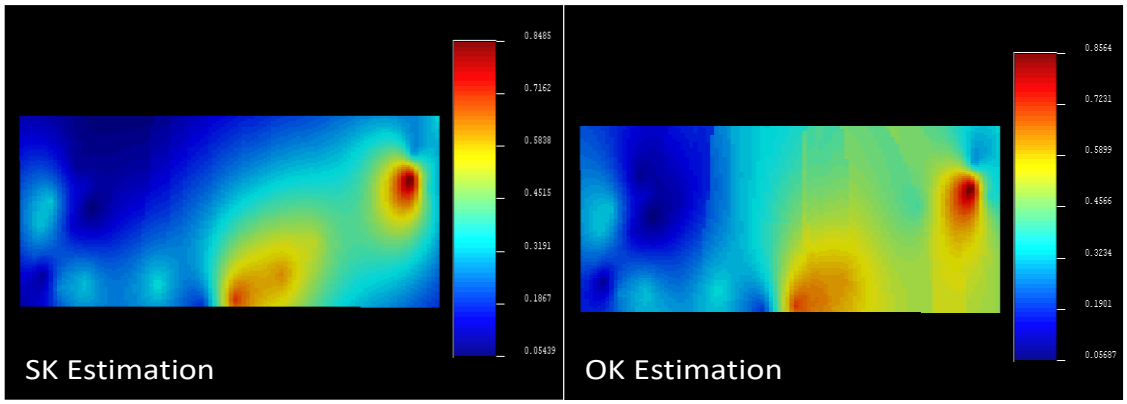

(c)

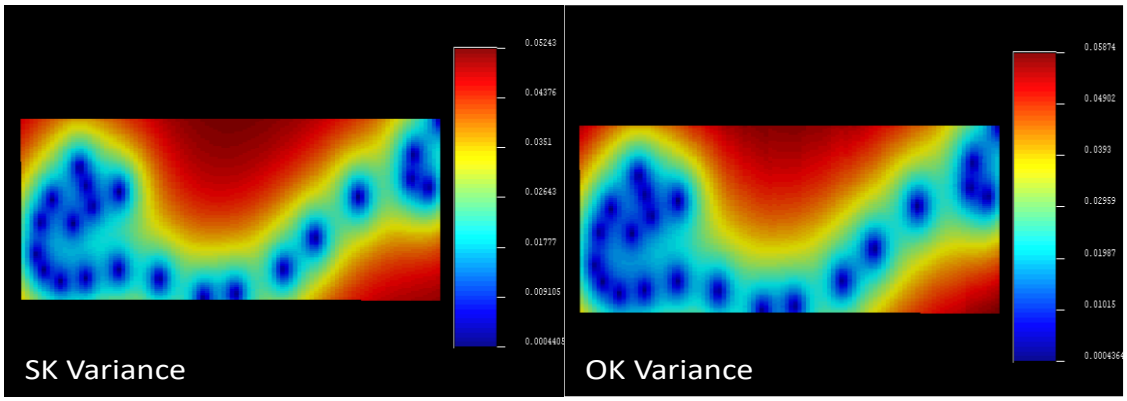

(d)

Figure A3: The statistics of TP3(6500) (a), its isotropy variogram model (b), and the temperature estimated using SK and OK methods (c), with their estimation variances (d).

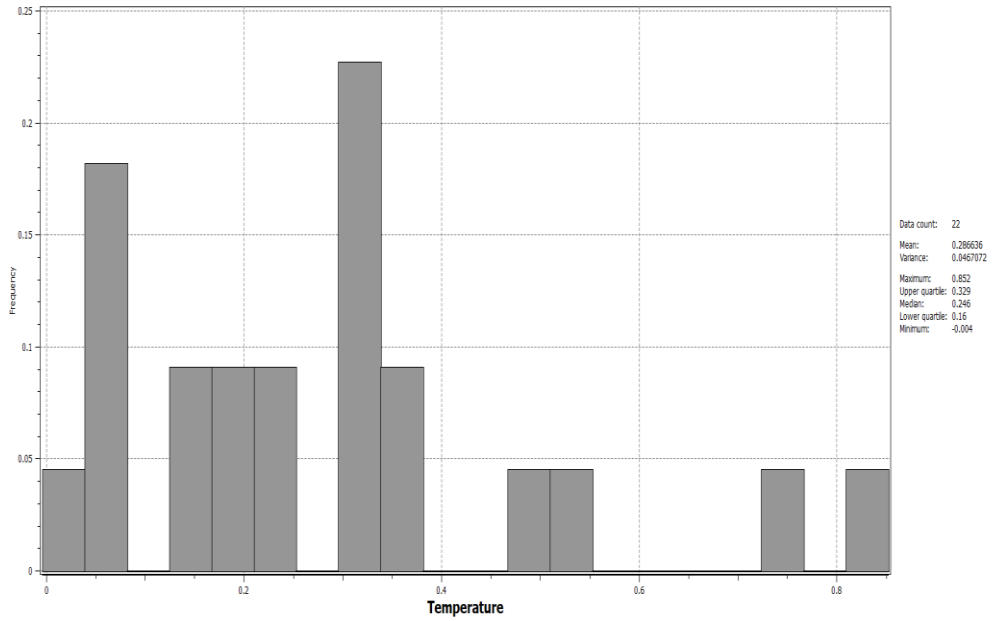

(a)

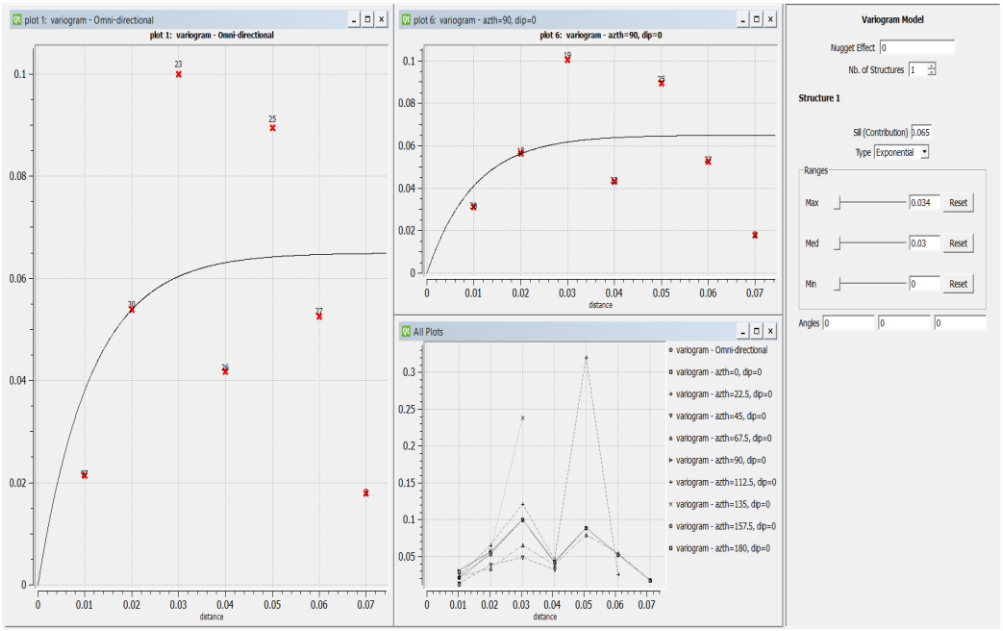

(b)

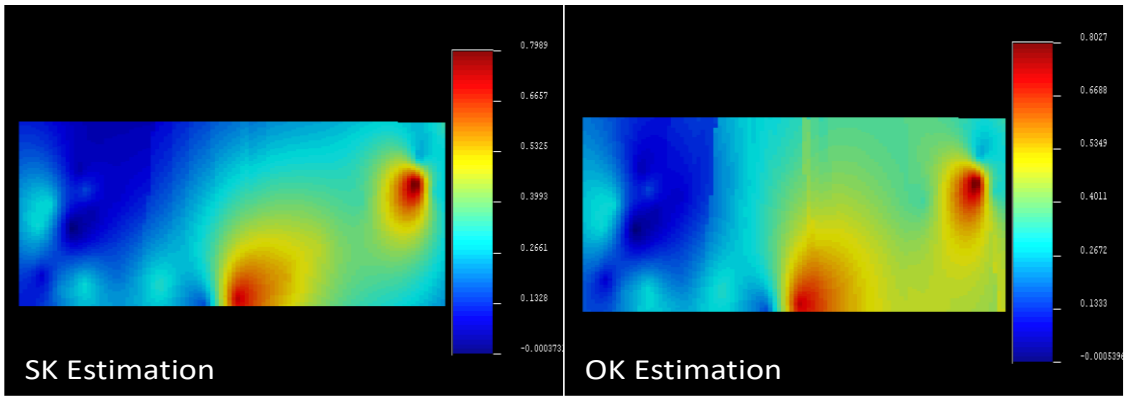

(c)

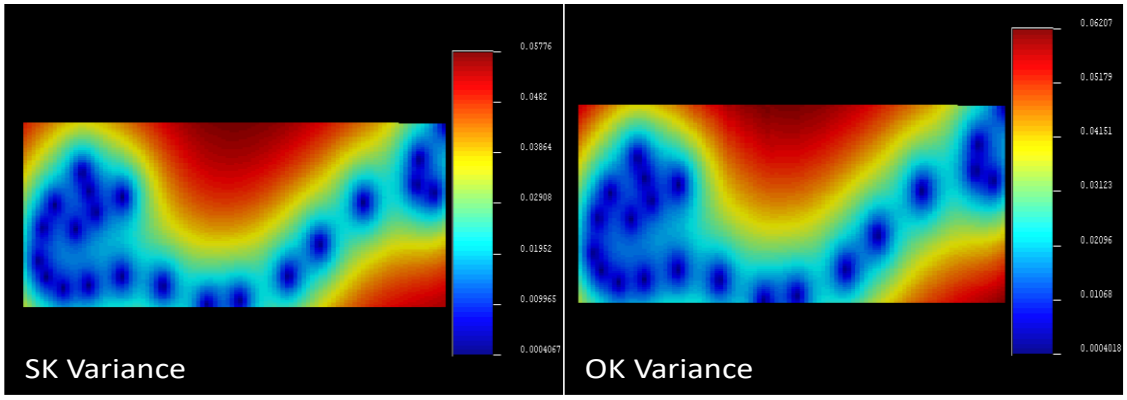

(d)

Figure A4: The statistics of TP4(7500) (a), its isotropy variogram model (b), and the temperature estimated using SK and OK methods (c), with their variances (d).

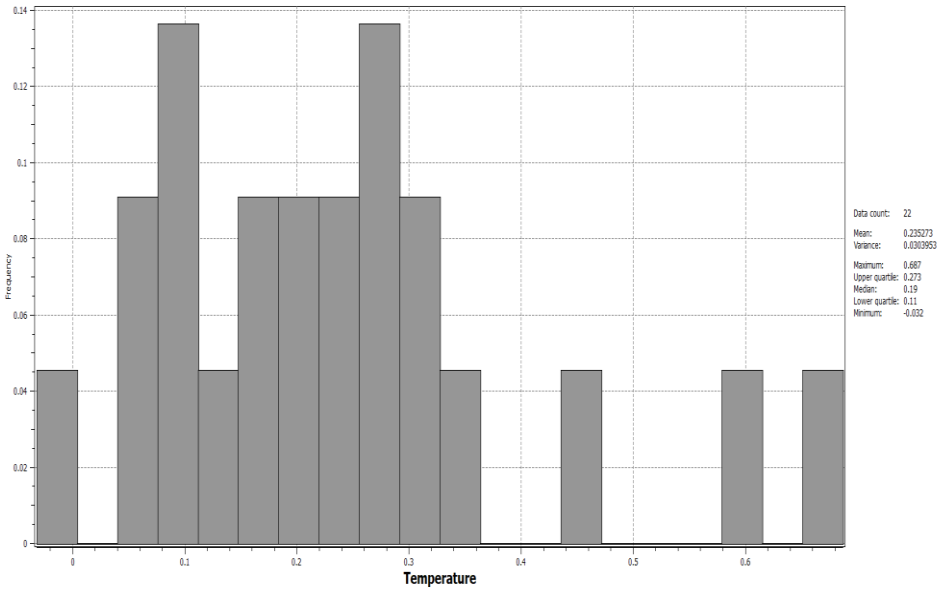
Frequency
Temperature
Data count: 22
Mean: 0.235273
Variance: 0.0303953
Maximum: 0.687
Upper quartile: 0.273
Median: 0.19
Lower quartile: 0.11
Minimum: -0.032

(a)

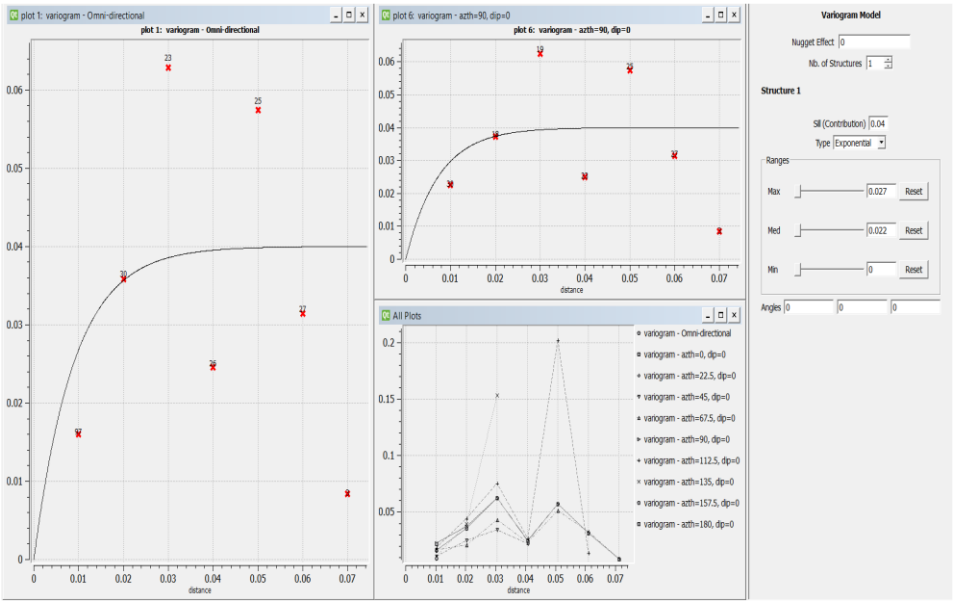
plot 1: variogram - Omni-directional
plot 6: variogram - azth=90, dip=0
All Plots
Variogram Model
Nugget Effect
Nb. of Structures
Structure 1
Sill (Contribution)
Type
Exponential
Ranges
Max
Med
Min
Reset
Angles
distance

(b)

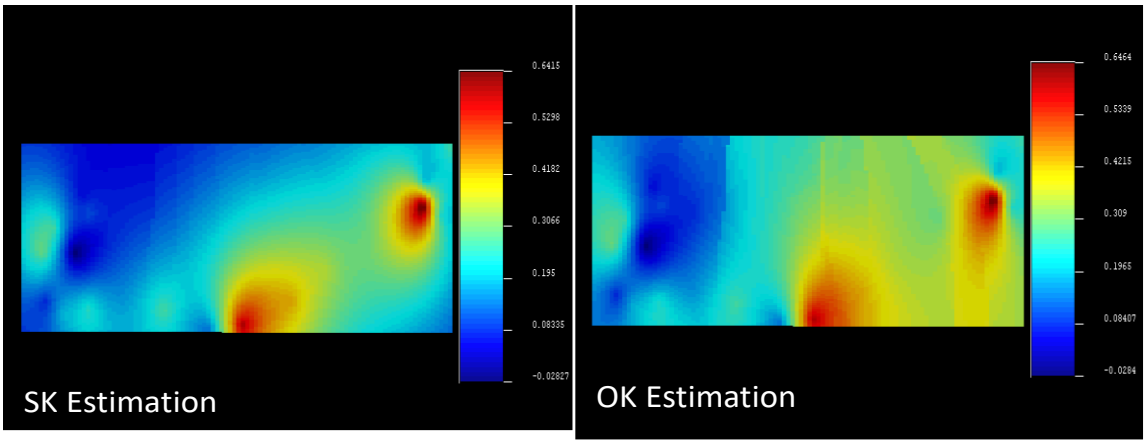
SK Estimation
OK Estimation

(c)

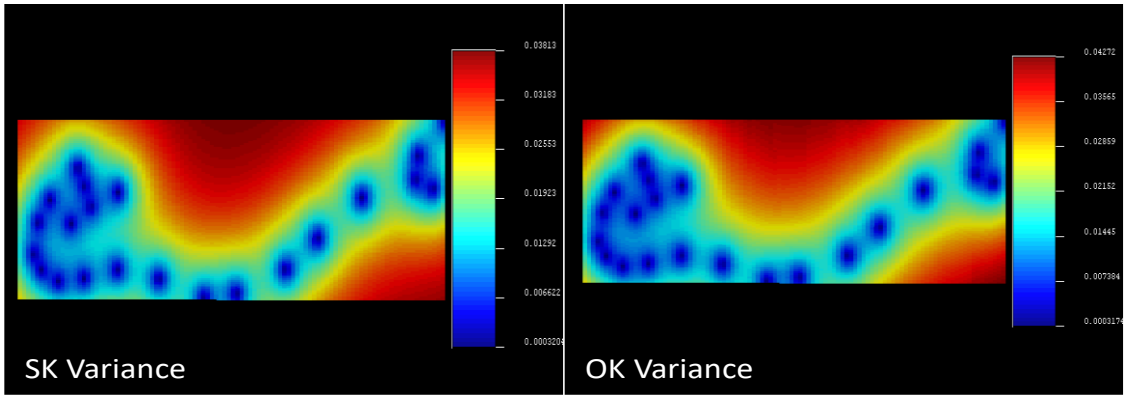

(d)

Figure A5: The statistics of TP5(8500) (a), its isotropy variogram model (b), and the temperature estimated using SK and OK methods (c), with their estimation variances (d).

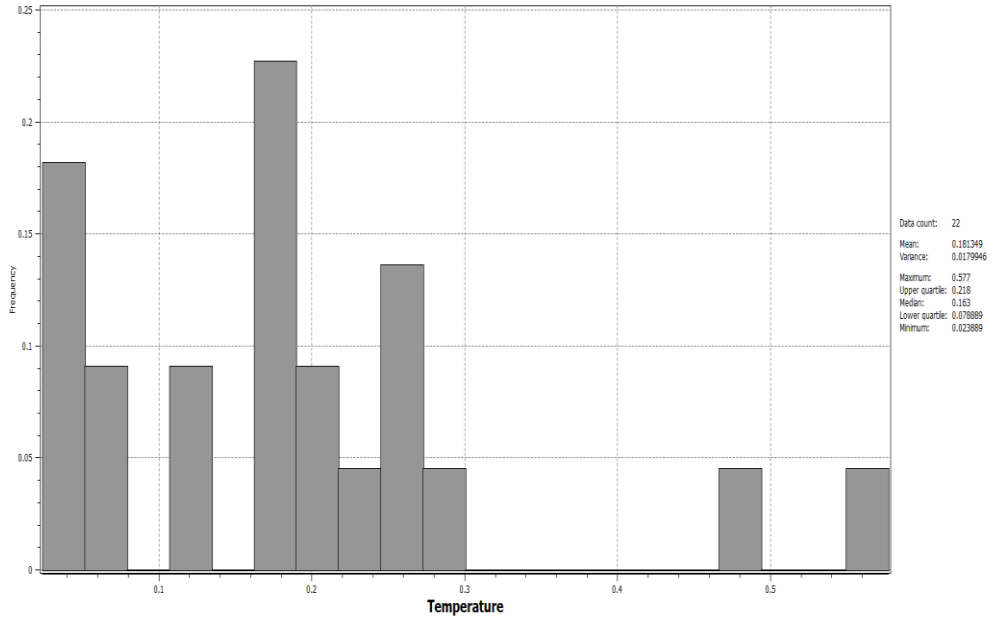

(a)

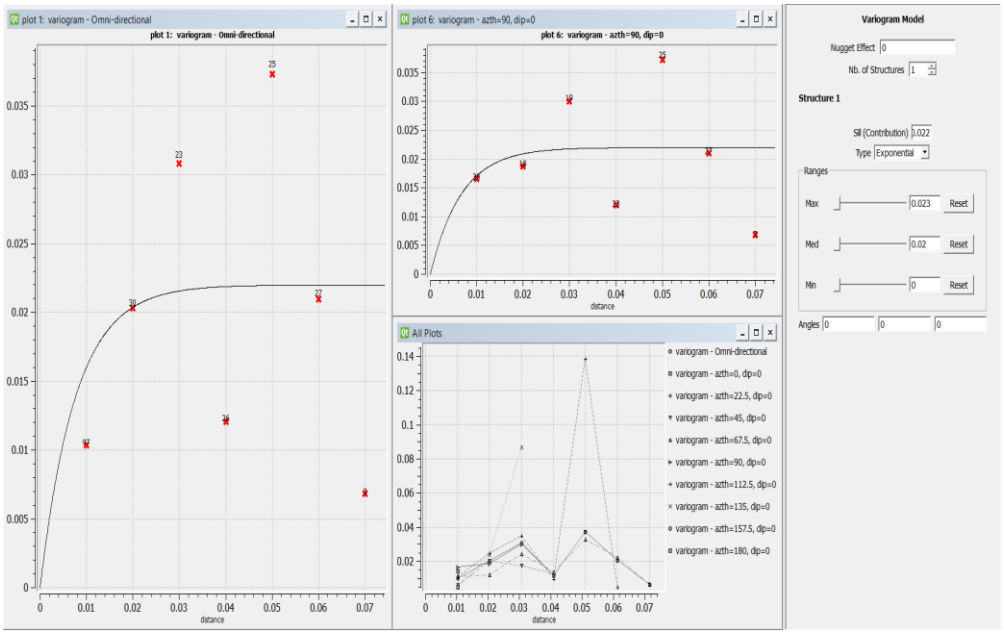

(b)

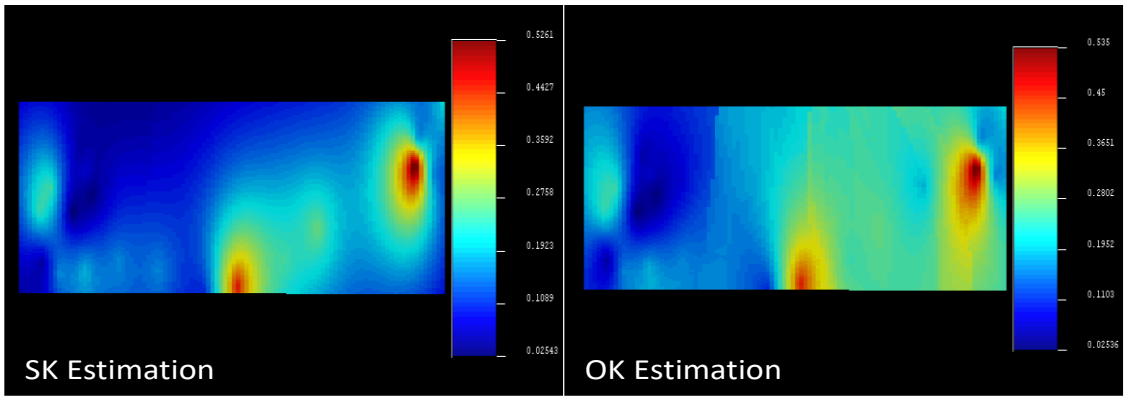

(c)

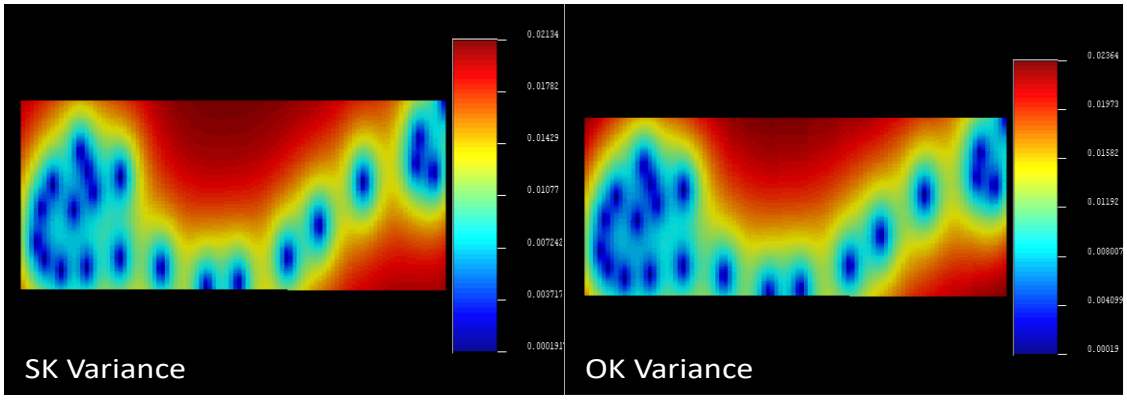

(d)

Figure A6: The statistics of TP6(9500) (a), its isotropy variogram model (b), and the temperature estimated using SK and OK methods (c), with their estimation variances (d).

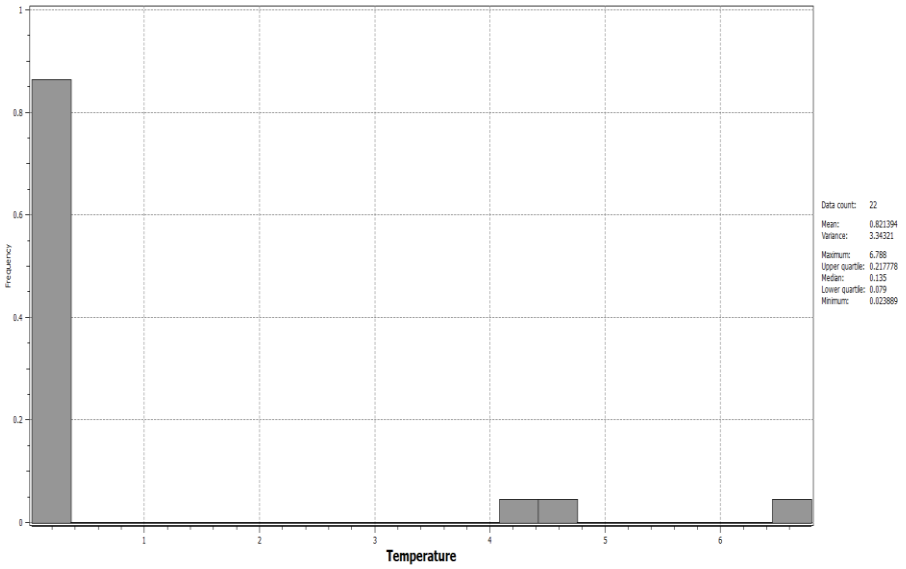
Frequency
Temperature
Data count: 22
Mean: 0.821394
Variance: 3.34321
Maximum: 6.788
Upper quartile: 0.217778
Median: 0.135
Lower quartile: 0.079
Minimum: 0.023889

(a)

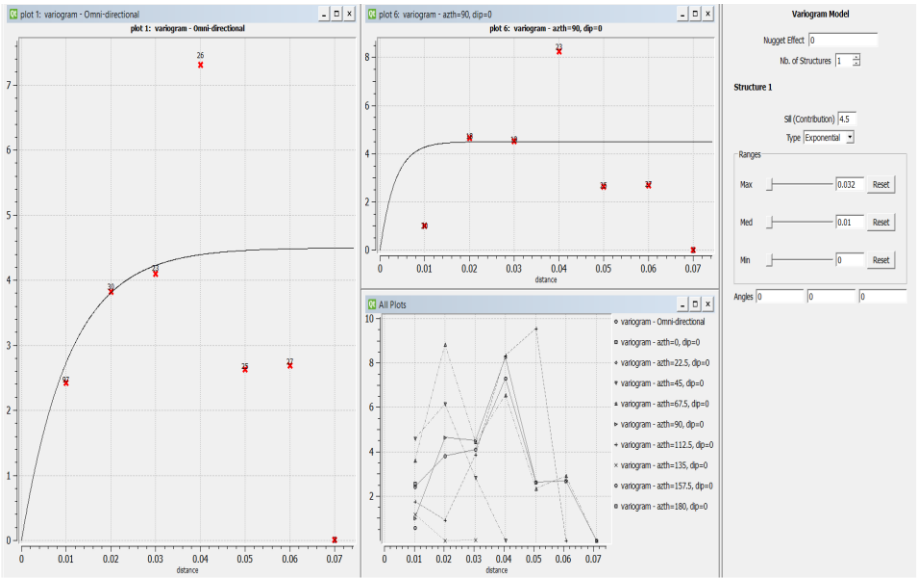
plot 1: variogram - Omni-directional
plot 6: variogram - azth=90, dip=0
All Plots
Variogram Model
Nugget Effect
Nb. of Structures
Structure 1
Sill (Contribution)
Type
Exponential
Ranges
Max
Med
Min
Angles
distance

(b)

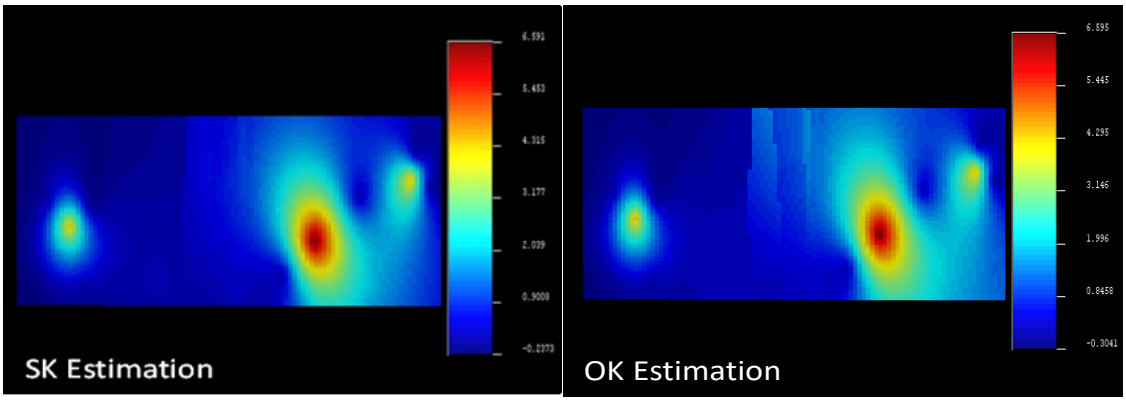
SK Estimation
OK Estimation

(c)

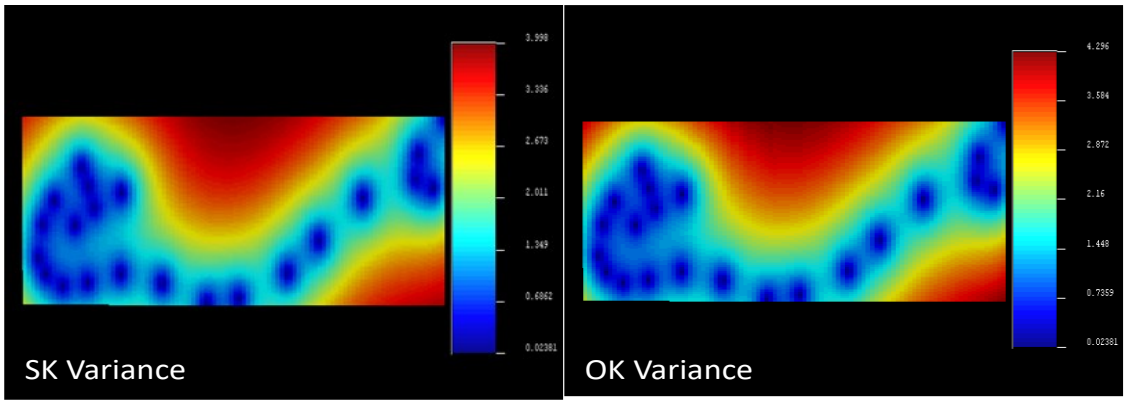

(d)

Figure A7: The statistics of TP7(10500) (a), its isotropy variogram model (b), and the temperature estimated using SK and OK methods (c), with their estimation variances (d).

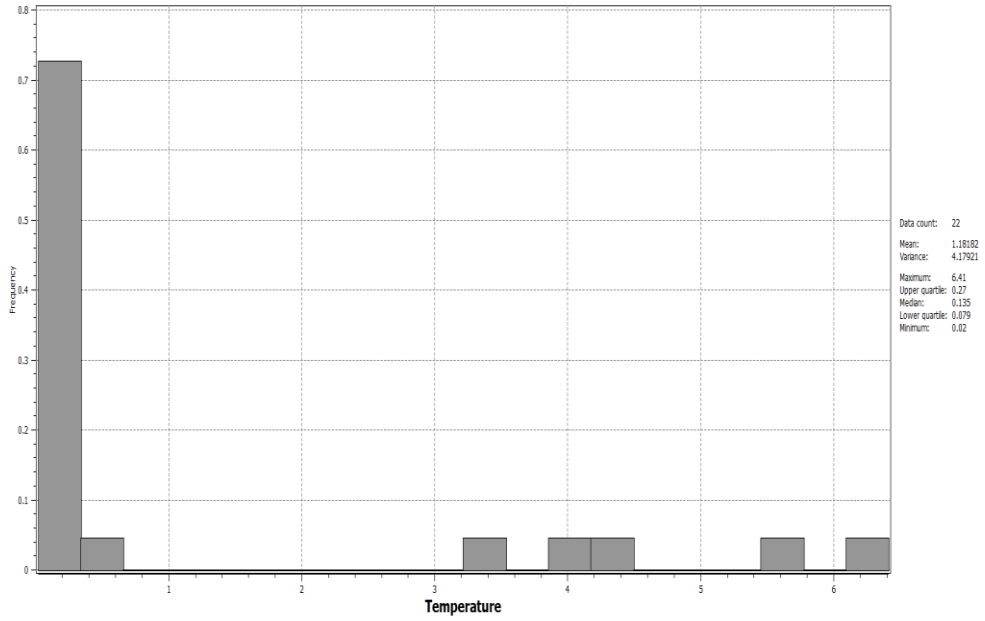

(a)

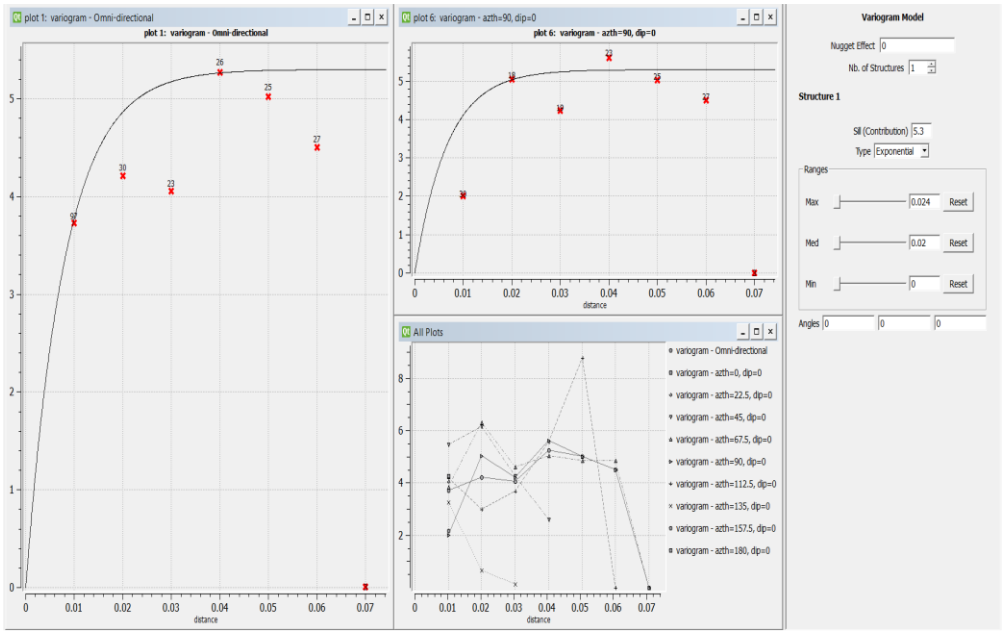

(b)

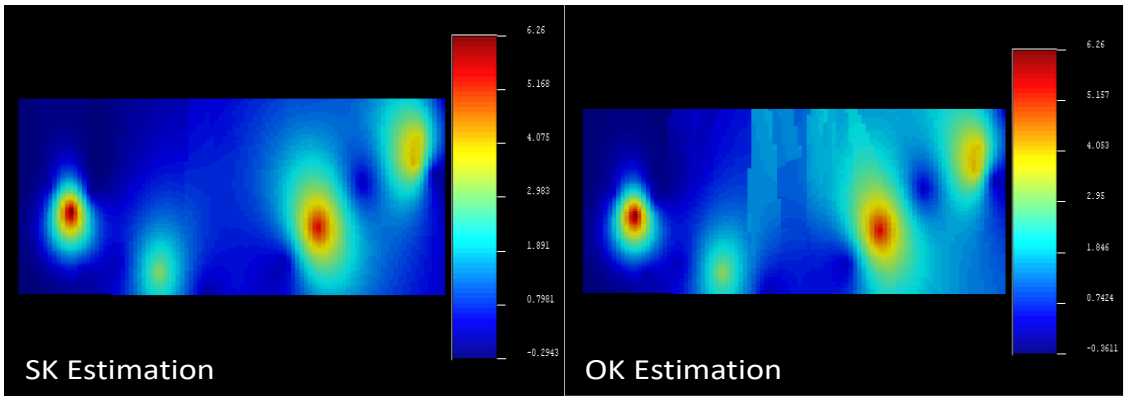

(c)

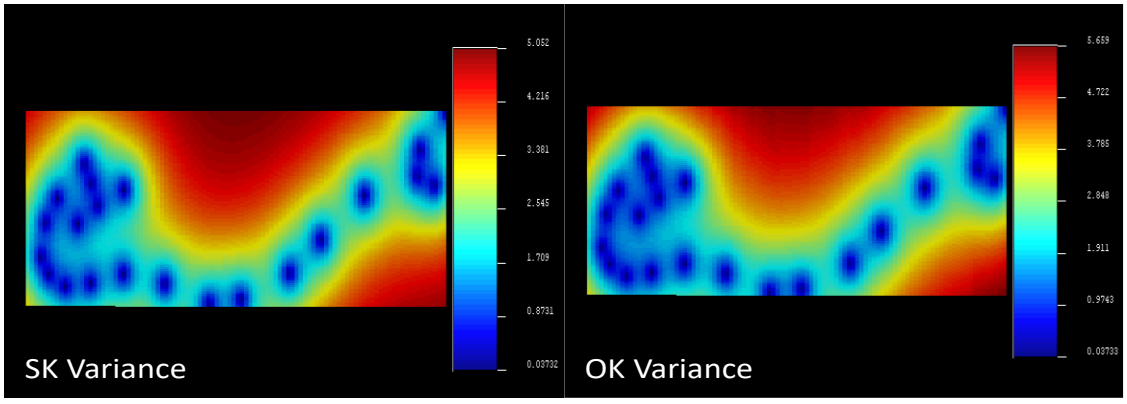

(d)

Figure A8: The statistics of TP8(10900) (a), its isotropy variogram model (b), and the temperature estimated using SK and OK methods (c), with their estimation variances (d).